



UNIVERSITY OF LEEDS

This is a repository copy of *Structure of the north-western North Anatolian Fault Zone imaged via teleseismic scattering tomography*.

White Rose Research Online URL for this paper:
<https://eprints.whiterose.ac.uk/175929/>

Version: Accepted Version

Article:

Rost, S orcid.org/0000-0003-0218-247X, Houseman, GA, Frederiksen, AW et al. (9 more authors) (Accepted: 2021) Structure of the north-western North Anatolian Fault Zone imaged via teleseismic scattering tomography. *Geophysical Journal International*. ISSN 0956-540X (In Press)

<https://doi.org/10.1093/gji/ggab265>

Reuse

Items deposited in White Rose Research Online are protected by copyright, with all rights reserved unless indicated otherwise. They may be downloaded and/or printed for private study, or other acts as permitted by national copyright laws. The publisher or other rights holders may allow further reproduction and re-use of the full text version. This is indicated by the licence information on the White Rose Research Online record for the item.

Takedown

If you consider content in White Rose Research Online to be in breach of UK law, please notify us by emailing eprints@whiterose.ac.uk including the URL of the record and the reason for the withdrawal request.



eprints@whiterose.ac.uk
<https://eprints.whiterose.ac.uk/>

Structure of the north-western North Anatolian Fault Zone imaged via teleseismic scattering tomography

S. Rost¹

G.A. Houseman¹

A. W. Frederiksen²

D. G. Cornwell³

M. Kahraman^{4,5}

S. Altuncu Poyraz⁵

U.M. Teoman⁵

D. A. Thompson^{1*}

N. Türkelli^{5†}

L. Gülen⁶

M. Utkucu⁶

T.J. Wright⁷

¹ *School of Earth and Environment, The University of Leeds, Leeds, LS2 9JT,*

² *Department of Geological Sciences, University of Manitoba, Winnipeg, Manitoba, Canada,*

³ *Department of Geology and Geophysics, School of Geosciences, University of Aberdeen, King's College, Aberdeen, AB*

⁴ *Eurasia Institute of Earth Sciences, Istanbul Technical University, Istanbul, Turkey*

⁵ *Kandilli Observatory and Earthquake Research Institute, Department of Geophysics, Boğaziçi University, 34684 Ceng*

⁶ *Department of Geophysical Engineering, Sakarya University, Esentepe Campus, 54187, Sakarya, Turkey*

⁷ *COMET, School of Earth and Environment, The University of Leeds, Leeds, LS2 9JT*

Received 2021 June 24 ; in original form 2020 August 18; Accepted 2021 June 29

SUMMARY

Information on fault zone structure is essential for our understanding of earthquake mechanics, continental deformation and seismic hazard. We use the scattered seismic wavefield to study the subsurface structure of the North-Anatolian Fault Zone (NAFZ) in the region of the 1999 İzmit and Düzce ruptures using data from an 18-month dense deployment of seismometers with a nominal station spacing of 7 km. Using the forward- and back-scattered energy that follows the direct *P*-wave arrival from teleseismic earthquakes, we apply a scattered wave inversion approach and are able to resolve changes in lithospheric structure on a scale of 10 km or less in an area of about 130 km by 100 km across the NAFZ. We find several crustal interfaces that are laterally incoherent beneath the surface strands of the NAFZ and evidence for contrasting crustal structures either side of the NAFZ, consistent with the presence of juxtaposed crustal blocks and ancient suture zones. Although the two strands of the NAFZ in the study region strike roughly east-west, we detect strong variations in structure both north-south, across boundaries of the major blocks, and east-west, parallel to the strike of the NAFZ. The surface expression of the two strands of the NAFZ is coincident with changes on main interfaces and interface terminations throughout the crust and into the upper mantle in the tomographic sections. We show that a dense passive network of seismometers is able to capture information

from the scattered seismic wavefield and, using a tomographic approach, to resolve the fine scale structure of crust and lithospheric mantle even in geologically complex regions. Our results show that major shear zones exist beneath the NAFZ throughout the crust and into the lithospheric mantle, suggesting a strong coupling of strain at these depths.

Key words: Seismology, Teleseismic Scattering, Tomography, North Anatolian Fault Zone.

1 INTRODUCTION

The North Anatolian Fault Zone (NAFZ) is one of the longest continuous continental strike slip fault systems on Earth, posing considerable hazard to Northern Anatolia and especially the megacity of Istanbul towards its western end. Here, we use a novel imaging technique using the scattered seismic wavefield in a tomographic approach to resolve the lithospheric structure within and below the NAFZ with the aim to better resolve the crustal structure around the fault zone and find evidence for shear zones at depth.

The NAFZ is a 1500 km long, right-lateral strike slip fault running the length of northern Anatolia, separating the Eurasian plate to the north from the deforming Anatolian region in the south, accommodating the relative motion and deformation between these tectonic domains. Together with the East Anatolian Fault, the NAFZ accommodates the westward motion of Anatolia (McKenzie, 1972; Reilinger et al., 2006; Şengör et al., 2005; Barka, 1992) driven by the gradient of gravitational potential energy from the Anatolian plateau to the Hellenic Trench (England et al., 2016).

The NAFZ ruptured in a series of $M \geq 6.7$ earthquakes during the 20th century from east to west (Stein et al., 1997), interpreted as stress transfer along the strike of the NAFZ from one earthquake bringing the next segment closer to failure. The two most recent events in the current series occurred in 1999 with epicentres in İzmit ($M=7.6$) and Düzce ($M=7.2$) (Barka et al., 2002; Gülen, 2002), with the fault rupture extending into the Sea of Marmara and the next anticipated event in the series posing a pronounced risk to the city of Istanbul.

* now at Omanos Analytics, Glasgow

† Deceased, April 2021

21 While the deformation at the surface is localized on faults (Hussain et al., 2016; Bürgmann &
22 Dresen, 2008), the distribution of deformation throughout the crust and into the mantle remains
23 unclear (Bürgmann & Dresen, 2008; Vauchez et al., 2012; Moore & Parsons, 2015). Understanding
24 the structure and dynamics of fault zones, especially at depth, is essential for our understanding of
25 continental deformation and seismic hazard.

26 Here, we aim to better understand the structure of the NAFZ, especially in the middle and
27 lower crust and into the upper mantle, using data from temporary seismic stations and exploit-
28 ing the scattered seismic wavefield following the *P*-wave arrivals of teleseismic events (Frederik-
29 sen & Revenaugh, 2004). We use data from the 18-month DANA deployment (DANA, 2012)
30 across the NAFZ in the region of the 1999 ruptures (Fig. 1a). The *P*-wave coda contains energy
31 from *P*-to-*P* and *P*-to-*S* scattering at small-scale heterogeneities along the ray-paths. Structure
32 can be recovered from the scattered seismic energy through migration approaches ranging from
33 common-conversion-point or common-scattering-point stacking (e.g. Dueker & Sheehan, 1997)
34 to full depth migration (e.g. Ryberg & Weber, 2000). Here we are using a tomographic waveform
35 approach based on linear inverse theory of the scattered wavefield (Ji & Nataf, 1998; Frederik-
36 sen & Revenaugh, 2004) to resolve the structure of the lithosphere and potential shear zones. The
37 scattering tomography builds on different principles than the more established *P*-receiver function
38 method previously applied to this dataset (Kahraman et al., 2015). With different resolution, limi-
39 tations and trade-offs this study will contribute to our knowledge of the fine-scale structure of the
40 lithosphere beneath this major fault zone.

41 We find that the two strands of the NAFZ evident in the shallow structure coincide with main
42 interfaces and interface terminations throughout the crust and into the upper mantle indicating that
43 the fault zone structure may extend to depths of at least ~ 75 km in this region. We find evidence
44 for small-scale variation of structure in the vicinity of the strands that might indicate the detection
45 of heterogeneity related to past deformation along the present day fault.

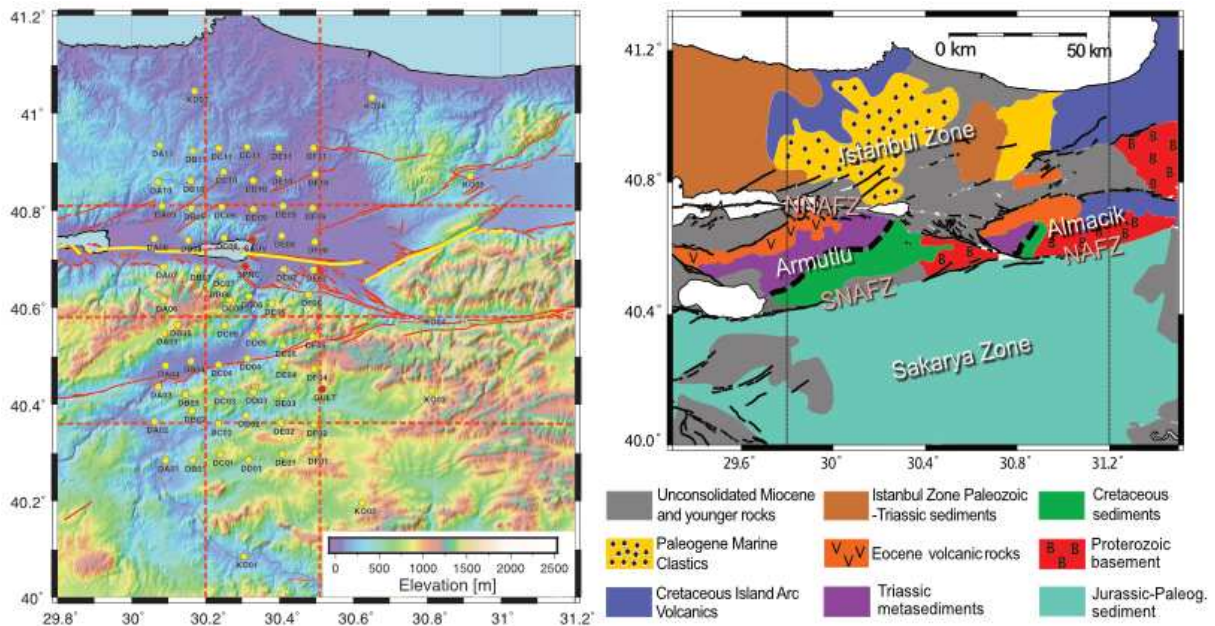


Figure 1. Study region. (a) Topographic map of the study region using SRTM data (Farr et al., 2007). Stations are indicated by yellow circles (permanent stations in red). Mapped faults (red lines) provided by Emre et al. (2018) and rupture of the 1999 İzmit and Düzce earthquakes (yellow) provided by Gülen (2002). Dashed north-south and east-west lines indicate location of depth profiles shown in Fig. 6 and 7 and are approximate locations of depth profiles provided by Kahraman et al. (2015). (b) Simplified geological map of the region outlining the three main tectonic blocks and geological areas. After Taylor et al. (2019a).

2 TECTONICS AND PREVIOUS GEOPHYSICAL SURVEYS

The study region (Fig. 1b) is an amalgam of continental and subduction-related oceanic fragments that remain after the closing of the Tethyan Ocean in the late Tertiary (e.g. Okay et al., 2008; Robertson & Ustaömer, 2004). The DANA network samples three tectonic blocks situated in the study region (i) The Istanbul-Zonguldak Zone (IZ) to the north of the northern strand of the NAFZ, (ii) the Sakarya zone (SZ) to the south of the southern strand; and (iii) the Armutlu and Almacik blocks (AA). The NAFZ splays into a northern (NNAFZ) and southern (SNAFZ) strand west of about 30.65° , with the NNAFZ and the SNAFZ following the northern and southern boundary of the AA. The AA is interpreted as the cause for the splay (e.g. Akbayram et al., 2016). The NAFZ is co-located with the intra-Pontide suture for at least half its onshore length and the boundaries between the SZ, AA, and IZ likely represent the suture in this locale (e.g. Okay et al., 2008). The NAFZ is believed to have developed ~ 11 Ma ago in eastern Anatolia with strain localisation

58 propagating westward and reaching the Sea of Marmara, and our study region, before 3.9 Ma
59 (Akbar et al., 2016). Slip on the northern and southern NAFZ strands has been estimated
60 to be approximately 16-25 mm/yr and 5-19 mm/yr, respectively (Stein et al., 1997; Flerit et al.,
61 2003; Meade et al., 2002). The northern branch of the NAFZ in our study area last ruptured in
62 the 1999 İzmit earthquake (Tibi et al., 2001; Barka et al., 2002) and still shows active slip at the
63 surface (Hussain et al., 2016) although current seismicity is not focussing beneath either fault
64 strand (Altuncu Poyraz et al., 2015).

65 The crustal structure in our study region has been characterised using a wide variety of geo-
66 physical techniques including seismic refraction (Karahan et al., 2001; Horasan et al., 2002; Bekler
67 & Gürbüz, 2008), ambient noise (Taylor et al., 2016, 2019a), receiver functions (Vanacore et al.,
68 2013; Kahraman et al., 2015; Jenkins et al., 2020), local earthquake tomography (Bariş et al., 2005;
69 Koulakov et al., 2010; Beyhan & Alkan, 2015; Polat et al., 2016; Yolsal-Çevikbilen et al., 2012),
70 magnetotellurics (Tank et al., 2005), and regional full waveform tomography (Fichtner et al., 2013;
71 Çubuk-Sabuncu et al., 2017). Similarly, the upper mantle has been studied using receiver functions
72 (Kind et al., 2015; Taylor et al., 2019b), seismic anisotropy (Biryol et al., 2010; Paul et al., 2014;
73 Lemnifi et al., 2017; Legendre et al., 2021) and body and surface wave tomography (Berk Biryol
74 et al., 2011; Bakırcı et al., 2012; Salaün et al., 2012; Fichtner et al., 2013; Govers & Fichtner,
75 2016; Papaleo et al., 2017, 2018).

76
77 The study region has been sampled by two seismic refraction experiments crossing all major
78 tectonic blocks, finding crustal thicknesses of 32 ± 2 km at about 30.10° longitude in the east
79 (Bekler & Gürbüz, 2008) and ≈ 38 km at about 29.25° longitude in the west of our study region
80 (Karahan et al., 2001). The refraction data show evidence for a 5 km thick upper crustal layer
81 with P -wave velocities (V_P) of 5.6 to 6.1 km/s and lower crustal velocities of $V_P = 6.7 - 7.2$
82 km/s (Bekler & Gürbüz, 2008). The upper mantle between 29.5° and 30.0° E is relatively slow
83 ($V_P = 7.6$ km/s) (Bekler & Gürbüz, 2008), while Karahan et al. (2001) find higher mantle velocities
84 further east (29.0° to 29.5° E) with velocities of $V_P \approx 8.1$ km/s. There is evidence for seismic
85 discontinuities at crustal depths of ≈ 17 km and ≈ 24 km (Karahan et al., 2001).

86 A study using local earthquake waveforms (Horasan et al., 2002) finds a Moho depth of 32 km
87 in the Marmara region. They find crustal discontinuities at 4 km and 17 km depth with upper
88 mantle velocities of 8.0 km/s and 4.6 km/s for V_P and V_S , respectively and mantle densities of
89 3.4 g/cm^3 . Upper crustal velocities are found to be 5.8 km/s and 3.4 km/s, lower crustal velocities
90 of 6.2 km/s and 3.6 km/s and near-surface velocities of 3.5 km/s and 2.2 km/s for V_P and V_S ,
91 respectively (Horasan et al., 2002).

92 Using fault zone head waves and fault zone reflected waves from seismicity and stations close
93 to the fault zone it is possible to resolve the interface properties of the fault zone. Ben-Zion &
94 Sammis (2003) and Ben-Zion et al. (2003) imaged a shallow fault zone extending about 3 – 4 km
95 into the crust with velocity reductions of up to 50% but a width of only 100 m, well below the
96 resolution of most other seismic methods. In the area of the 1999 Düzce and İzmit earthquakes
97 Bulut et al. (2012) and Najdahmadi et al. (2016) image the material properties across the fault zone
98 using trapped waves and find a bimaterial interface down to the base of the seismogenic crust with
99 an average velocity contrast of 3.4% (Najdahmadi et al., 2016) and 6% with the southern block
100 being fast (Bulut et al., 2012).

101 Studies of local earthquakes detect upper crustal anisotropy around the NAFZ, limiting it to
102 the upper 8 km (Hurd & Bohnhoff, 2012) or 4 km (Peng & Ben-Zion, 2004), likely due to aligned
103 cracks in the uppermost crust. Detected splitting times are on the order of 10 ms not likely in-
104 fluencing the results of this study. SKS analysis detects asthenospheric anisotropy (Biryol et al.,
105 2010; Paul et al., 2014; Legendre et al., 2021) with lag times between fast and slow direction of
106 typically $1.5 \pm 0.4 \text{ s}$ with fast polarization directions smoothly varying from NNE–SSW in northern
107 Turkey to NE–SW in eastern Turkey. A combined study of shear-wave splitting and anisotropic
108 receiver functions show complex anisotropy especially in our study region (Lemnifi et al., 2017).
109 Shear-wave splitting tomography using aftershocks of the 1999 İzmit and Düzce earthquakes show
110 a 3 km wide anisotropic zone extending to 5 km depth with distinct asymmetry being related to
111 damage from the unilateral eastward propagation of the 1999 İzmit rupture (Li et al., 2014).

112 P -wave receiver functions (PRFs) east of the Sea of Marmara indicate a deepening of the
113 Moho from west (29 to 32 km) to east (34 to 35 km) (Zor et al., 2003; Vanacore et al., 2013). The

114 average crustal V_P/V_S in our study region is ~ 1.75 (Vanacore et al., 2013). PRFs of the DANA
115 dataset (Kahraman et al., 2015) find crustal thickness and V_P/V_S variation in both EW and NS
116 directions with the crust deepening from 36.5 km ($V_P/V_S = 1.73$) to 40 km ($V_P/V_S = 1.73$) in
117 the IZ, a constant crustal thickness of ~ 37 km ($V_P/V_S = 1.69$ to 1.70) in the AA, and a slight
118 thinning from ~ 35 km ($V_P/V_S = 1.73$) in the west to ~ 34 km ($V_P/V_S = 1.85$) in the east of the
119 SZ (Fig. 1). Combining data from several permanent stations and temporary station deployments,
120 including DANA data, Jenkins et al. (2020) determined Moho depths across the Sea of Marmara
121 region finding thick crust of up to 41 km in the IZ, with a shallower Moho (32 – 34 km) in the
122 AA and SZ with evidence of discontinuous structure across the NAFZ. The transition also shows
123 complex Moho structure around the NNAFZ. Additionally, Jenkins et al. (2020) find east-west
124 variation with a general deepening of the Moho towards the east.

125 Previous studies evidence strong crustal heterogeneity on scales of less than 10 km with sharp
126 truncations of sub-horizontal interfaces coinciding with the surface locations of the northern and
127 southern NAFZ strands. The northern strand seems to penetrate deeper into the crust and may
128 extend into the upper mantle based on analysis of receiver functions and ambient noise cross-
129 correlations (Kahraman et al., 2015; Taylor et al., 2016; Jenkins et al., 2020). Both structural
130 changes in North-South and East-West direction have been reported (e.g. Kahraman et al., 2015;
131 Çubuk-Sabuncu et al., 2017; Jenkins et al., 2020).

132 Using P -wave transfer functions and a grid-search inversion approach Frederiksen et al. (2015)
133 detected a sharp change of crustal thickness across the northern NAFZ which is believed to follow
134 the trace of the Intra-Pontide suture in this location and a change of the V_P/V_S ratio across the
135 southern branch indicating a change in basement composition. The IZ shows thick crust (40 to
136 45 km) but low topography indicating that it is in isostatic disequilibrium or underlain by thicker
137 lithosphere, a result supported by Jenkins et al. (2020). The transfer functions also provide evi-
138 dence for thick sediments in the Sakarya and Pamukova basins in agreement with ambient noise
139 analysis (Taylor et al., 2019a).

140 Tomographic studies using traveltimes from local, regional and teleseismic events (e.g. Barış
141 et al., 2005; Salah et al., 2007; Koulakov et al., 2010; Bakırcı et al., 2012; Beyhan & Alkan,

142 2015; Polat et al., 2016; Papaleo et al., 2017, 2018) and full waveform information (e.g. Fichtner
143 et al., 2013; Govers & Fichtner, 2016; Çubuk-Sabuncu et al., 2017; Blom et al., 2020) find strong
144 velocity contrasts in the crust along the NNAFZ and the SNAFZ. These are interpreted as the fault
145 zone exploiting the sutures between the Istanbul zone, Armutlu block and Sakarya Zone as result
146 of the closure of the Neo-Tethys ocean. Nonetheless, Fichtner et al. (2013) note the lack of a low
147 velocity fault zone signature at depth west of $\sim 32^\circ$ E due to the absence of a well-localised suture
148 and insufficient strain localization due to the young age of the fault zone. In contrast, Koulakov
149 et al. (2010) using local tomography note the juxtaposition of high-velocity, low attenuation blocks
150 (e.g. Armutlu block) to lower velocity areas. A smaller scale, full waveform tomographic study
151 has been performed by Çubuk-Sabuncu et al. (2017) noticing strong lateral and vertical velocity
152 variations and strong radial anisotropy of the crust in agreement with the active tectonics of western
153 Turkey. Salah et al. (2007) focus on the rupture area of the 1999 İzmit and Düzce earthquakes
154 using local tomography to resolve P - and S -wave velocity as well as the Poisson ratio and detect
155 prominent low velocity zones down to depths of 25 km as well as well as a high-velocity anomaly
156 at a depth of 8 km between 30.0 and 30.4° E along the strike of the fault zone. Seismicity is more
157 prevalent in the high-velocity region although it also occurs in low velocity regions. Similarly,
158 traveltimes tomography resolves narrow sub-vertical low velocity zones coinciding with the surface
159 expression of the SNAFZ and the NNAFZ (Papaleo et al., 2017, 2018).

160 Magnetotelluric (MT) data show differences in the crustal conductivity from south to north
161 across the NAFZ (Tank et al., 2005) with a high resistivity ($\geq 1000 \Omega\text{m}$) crustal basement in the
162 IZ to the north and a less resistive crustal basement ($500 \Omega\text{m}$) in the SZ. The MT data resolve a
163 localized conductive zone (30 to $50 \Omega\text{m}$) within the AA that extends into the upper mantle that has
164 been attributed to partial melts or pore fluid flow from the upper mantle beneath the NAFZ.

165 3 METHOD

166 We apply the teleseismic scattering tomography approach by Frederiksen & Revenaugh (2004)
167 to the DANA dataset to resolve the small-scale structure beneath the array. The scattered seis-
168 mic wavefield is more sensitive to short-wavelength variations in material properties than is the

169 path-integrated sensitivity of transmitted phases such as used in e.g. seismic traveltime tomogra-
170 phy. The *P*-to-*p* and *P*-to-*s* scattered energy in the coda of teleseismic *P*-waves travelling along
171 different paths to the main arrival can uniquely determine Earth structure if the sampling of the
172 seismic wavefield is dense enough to avoid spatial aliasing. In the tomographic approach some
173 aliasing can be accepted without introducing issues with non-uniqueness of the solution due to
174 the regularization of the problem. Several approaches to use the scattered coda energy to image
175 the subsurface have been developed, forming a continuous spectrum of method complexity. The
176 common approach of receiver function analysis uses stacked records of *P*-to-*s* (or *S*-to-*p*) scattered
177 (converted) energy (Vinnik, 1977; Langston, 1979) which may be binned according to their com-
178 mon conversion point to improve signal-to-noise ratio (Dueker & Sheehan, 1997) and mapped to
179 depth. The method assumes a 1D stratified seismic structure which is often violated in practice
180 (Rondenay, 2009). Lateral variation of structure leads to diffraction of the seismic wavefield and
181 diffraction stacking, a backprojection of the diffracted energy along its traveltime hyperbola, can
182 be used to image small-scale perturbations on the order of the seismic wavelength of the structure
183 at depth. These methods are widely used in controlled-source applications (Yilmaz, 2001), and
184 are commonly described as migration techniques (Rondenay, 2009) but implementation requires
185 dense spatial sampling of the seismic wavefield. General improvements and densification of recent
186 passive seismic deployments make the application of more complex methods, such as traveltime
187 stacking of the scattered wavefield (Revenaugh, 1995) or the application of inversion or backpro-
188 jection operators in a 2D or 3D model space (Bostock & Rondenay, 1999) possible and allow
189 higher resolution of detail. For a full review of these methods see Rondenay (2009).

190

191 For a more complete treatment of the scattering problem, the scattering image problem can be
192 formulated as a tomographic inversion (Ji & Nataf, 1998). Using a waveform inversion, Frederik-
193 sen & Revenaugh (2004) have developed a linear tomographic inversion of the scattered seismic
194 wavefield which we apply here. A full description is given in Frederiksen & Revenaugh (2004)
195 and we outline only the main points of this approach here.

196 The Born approximation, a common approximation of the full scattering process, assumes a

197 weakly scattering medium and single scattering (Sato et al., 2012), which is a good approximation
 198 for this application where the amplitudes of the scattered wavefield are much smaller than those of
 199 the direct wave. In this approximation the scattering properties are represented as perturbations in
 200 elastic parameters ($\delta\lambda$, $\delta\mu$, $\delta\rho$) to a background model (λ_0 , μ_0 , ρ_0). The seismic equation of motion
 201 for the displacement u in an isotropic medium is given by:

$$\rho\ddot{u}_i = (\lambda\nabla \cdot \mathbf{u})_{,i} + [\mu(u_{i,j} + u_{j,i})]_{,j} \quad (1)$$

202 with λ and μ being the Lamé parameters and ρ the density. Eq 1 can be expanded, using small
 203 perturbations to the elastic properties ($\delta\lambda$, $\delta\mu$, $\delta\rho$) around a background medium with elastic prop-
 204 erties λ_0 , μ_0 , ρ_0 (Frederiksen & Revenaugh, 2004), to:

$$\begin{aligned} \rho_0\ddot{u}_i - (\lambda_0 + \mu_0)(\nabla \cdot \mathbf{u})_{,i} = \\ - \delta\rho\ddot{u}_i + (\delta\lambda + \delta\mu)(\nabla \cdot \mathbf{u})_{,i} + \delta\mu\nabla^2 u_i \\ + (\delta\lambda)_{,i}(\nabla \cdot \mathbf{u}) + (\delta\mu)_{,j}(u_{i,j} + u_{j,i}) \end{aligned} \quad (2)$$

205 The wavefield can then be divided into a primary (background) and scattered component ($\mathbf{u} =$
 206 $\mathbf{u}^0 + \delta\mathbf{u}$) with the unperturbed wavefield satisfying the unperturbed wave equation

$$\rho_0\ddot{u}_i^0 = (\lambda_0 + \mu_0)(\nabla \cdot \mathbf{u}^0)_{,i} + \mu_0 u_{i,jj}^0 \quad (3)$$

207 Assuming that the scattered wavefield is much weaker than the unperturbed wavefield this gives
 208 the first-order Born approximation by discarding higher-order terms:

$$\rho_0\delta\ddot{u}_i - (\lambda_0 + \mu_0)(\nabla \cdot \delta\mathbf{u})_{,i} - \mu_0\nabla^2\delta u_i = Q_i \quad (4)$$

209 with Q_i being a term of the unperturbed wavefield and the perturbed model parameters which is
 210 given by equation 13.22 in Aki & Richards (2002):

$$Q_i = -\delta\rho\ddot{u}_i^0 + (\delta\lambda + \delta\mu)(\nabla \cdot \mathbf{u}^0)_{,i} + \delta\mu\nabla^2 u_i^0 + (\delta\lambda)_{,i}(\nabla \cdot \mathbf{u}^0) + (\delta\mu)_{,j}[u_{i,j}^0 + u_{j,i}^0] \quad (5)$$

with \mathbf{u}^0 being a solution for the unperturbed medium.

Assuming Rayleigh scattering, where the wavelength of the incident wavefield is much larger than the scale of the heterogeneity, the scattering problem reduces to a point scatterer and the full scattered wavefield is approximated by that of an array of point scatterers. Following Wu & Aki (1985), it is possible to derive expressions for the equivalent point source in Rayleigh scattering. These expressions also contain the directivity of the radiation of the scattered wavefield, and are provided as equations (7) to (10) in Frederiksen & Revenaugh (2004). This gives us the ability to compute both the amplitude and radiation pattern of scattering from small-scale heterogeneities in solving the forward problem of the waveform inversion.

We assume the incident P -wave to be planar (Fig. 2) with a known slowness vector, a condition well met for teleseismic records. The scattered wavefield is derived from the seismic observations by computing the 3-component receiver functions relative to the first arriving P wave. The considered input seismic wavefield includes the direct incident P and the free-surface reflections (Pp and Ps), producing forward- and back-scattering in the volume, respectively. The forward and backscattering of the input wavefield produces six possible scattered phases (where \bullet indicates the scattering event along the raypath) at small-scale elastic heterogeneities: $P\bullet p$, $P\bullet s$, $Pp\bullet p$, $Pp\bullet s$, $Ps\bullet p$ and $Ps\bullet s$. In the forward modelling, we consider every possible combination of perturbed parameter (P - and S -wave velocity perturbation ($\delta\alpha$, $\delta\beta$) and density perturbation ($\delta\rho$)), incident wave (forward scattering P and backscattering free surface reflection Pp and Ps) and station location. The inclusion of the free surface backscattered energy as well as the forward scattered direct wave increases the resolution of the study volume and allows us to resolve a 3D perturbation model, here represented as a regular grid of perturbed cells. We use ray tracing in a 1D velocity model to determine traveltimes to and from the scattering heterogeneity and to calculate incidence and refraction angles. We use equations (7) to (10) of Frederiksen & Revenaugh (2004) including a geometrical spreading factor for a layered medium to determine the amplitudes of the scattered energy in an elastic velocity model.

The Born approximation prescribes that single scattered waves propagate in the unperturbed

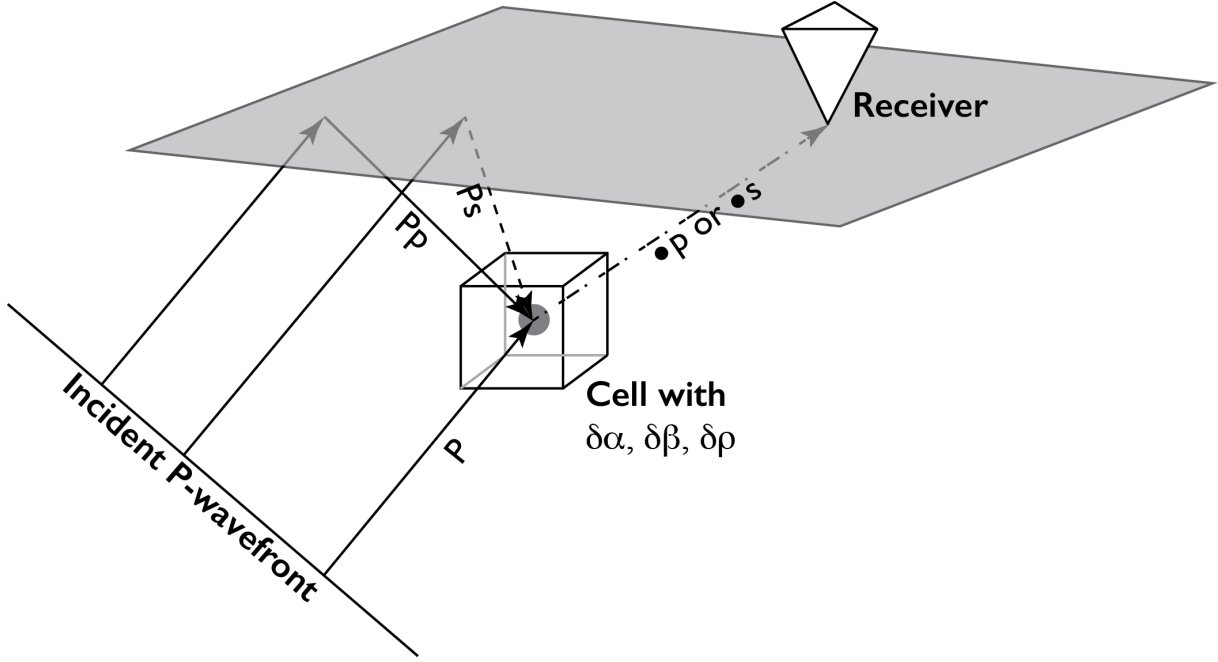


Figure 2. Sketch of the scattered phases included in the full waveform inversion. An incoming planar P-wave wavefront interacts with a cell with a parameter disturbance ($\delta\alpha$, $\delta\beta$, $\delta\rho$) either from the direct wavefront (forward scattered) or the back-scattered wave from the free-surface reflection. The wavetype can convert upon scattering from P to S.

239 medium and do not interact with heterogeneities again. Therefore, the scattered wavefields from
 240 individual heterogeneities are independent. The complete scattered wavefield T can therefore be
 241 obtained through the summation of the contributions of individual heterogeneities:

$$T = \sum_{i=1}^N \sum_{j=1}^3 t_{ij} \quad (6)$$

242 with t_{ij} representing the time series representing the scattering contribution of the j th perturbed
 243 parameter of the i th scatterer (Frederiksen & Revenaugh, 2004).

244 The medium beneath the array is parameterised into a 3D grid of cells with each cell potentially
 245 containing a perturbation of elastic parameters. The perturbation for all cells can be collapsed in
 246 an M -element vector \mathbf{m} with dimension $M = \# \text{ cells in } [x, y, z] \times \text{properties } [\delta\alpha, \delta\beta, \delta\rho]$. Summing
 247 over all contributing elements we obtain the N -element vector \mathbf{d}^i with the number of displacement
 248 samples depending on $N = \text{samples} \times \text{stations} \times \text{components} \times \text{events}$. The dependence of the
 249 full scattered wavefield on arbitrary model \mathbf{m} is then described as

$$\mathbf{d} = \mathbf{A}\mathbf{m} \quad (7)$$

250 \mathbf{A} is an $N \times M$ matrix describing the sensitivity of each data point to each model parameter, i.e.
 251 each column of \mathbf{A} represents a differential seismogram for a perturbation of a single parameter in
 252 a single cell of the perturbed model. Equation (7) is linear and can therefore be solved using linear
 253 inverse theory. To pose this problem as a damped inversion the inverse problem is formulated as a
 254 minimization:

$$\min \left\| \begin{bmatrix} \mathbf{A} \\ \lambda \mathbf{I} \end{bmatrix} \mathbf{m} - \begin{bmatrix} \mathbf{d} \\ 0 \end{bmatrix} \right\|_2 \quad (8)$$

255 with \mathbf{I} being an $M \times M$ identity matrix and λ a weighting factor, representing uniform damping. We
 256 use the LSQR method (Paige & Saunders, 1982) to solve for the material properties in \mathbf{m} . For the
 257 inversion of real data it has been found that regularisation by smoothing is preferable to damping
 258 (Frederiksen & Revenaugh, 2004) as it provides results with higher coherence. Using LSQR, the
 259 model is smoothed by posing $\mathbf{m} = \mathbf{S}\mathbf{x}$ with \mathbf{S} being a matrix containing a Gaussian smoother. We
 260 use $\mathbf{B} = \mathbf{A}\mathbf{S}$ and the minimization

$$\min (\|\mathbf{B}\mathbf{x} - \mathbf{d}\|^2 + \lambda^2 \|\mathbf{x}\|^2) \quad (9)$$

261 in which we solve for \mathbf{x} rather than \mathbf{m} (Van der Lee & Nolet, 1997; Frederiksen & Revenaugh,
 262 2004). For all recovery tests and real data inversions, we apply a moving Gaussian smoother with
 263 a standard deviation of one model element in the horizontal directions, but we do not smooth in the
 264 vertical direction. No smoothing is applied beyond three standard deviations. This choice biases
 265 the recovered model towards lateral coherence, making recovered lateral changes more coherent in
 266 our study region where we expect strong lateral changes across the NAFZ. The smoothing limits
 267 lateral resolution of structures to about 10 km. Vertical resolution of 2 km is defined by the model
 268 discretization.

269 The model space is parameterised as a regular grid with 5 km horizontal grid spacing and 2 km

270 vertical grid spacing with 30 (0-29) cells in horizontal directions and 60 (0-59) in vertical direction.
 271 Each cell is treated as a point scatterer with vertical and horizontal locations at depths $2 \cdot j$ km ($j =$
 272 $0, \dots, 59$) and longitude/latitude location of $5 \cdot k$ ($k = 0, \dots, 29$), respectively. The maximum grid
 273 size is controlled by the maximum memory required to invert the dataset (see below). We tested the
 274 method with doubled lateral and vertical grid spacing and do not find noticeable differences in the
 275 general structure of the solutions except for obvious impacts on the maximum possible resolution
 276 of the solutions.

277 **4 DATA**

278 We use passive seismic data from stations of the Dense Array for Northern Anatolia (DANA)
 279 that were installed across the NAFZ in the region of the 1999 İzmit and Düzce ruptures (DANA,
 280 2012). DANA was deployed between May 2012 and October 2013 and stations were arranged in
 281 a quasi-rectangular region of 35 km by 70 km with a nominal station spacing of 7 km (Fig. 1).
 282 Stations were aligned along seven north-south oriented lines (labelled A to F) and 11 east-west
 283 lines (labelled 01 to 11). Seven additional stations were installed in an eastern semi-circle with
 284 a radius of about 60 km. Three permanent stations (SPNC, SAUV, GULT) of Boğaziçi Univer-
 285 sity and Kandilli Observatory and Earthquake Research Institute/National Earthquake Monitoring
 286 Center (BU-KOERI/NEMC) located within the DANA network grid were included in the analy-
 287 sis. Stations were equipped mainly with Güralp CMG-6TD and CMG-3T medium broadband and
 288 broadband three-component instruments (full information on the network can be found in DANA
 289 (2012)). Data were sampled at 50 Hz.

290 We use earthquakes within the deployment period with $m_b > 5.5$ from the catalogue of the
 291 National Earthquake Information Centre (NEIC) and angular distances of 30° to 90° . For the
 292 permanent stations we add events from 2009 onwards (in total 47 additional events contribut-
 293 ing typically a single 3-component seismogram (ZRT) to the dataset). Low frequency noise was
 294 suppressed by applying a 2-way, 2-pole high-pass filter with cut-off frequency of 0.1 Hz. We cal-
 295 culate 3-component receiver functions (RFs) with a maximum frequency of 1.2 Hz using the time
 296 domain iterative deconvolution approach by Ligorría & Ammon (1999) deconvolving the Z com-

ponent from the vertical, radial and transverse components. The calculated receiver functions were visually inspected to select events following these criteria: (1) transverse RFs show lower or comparable amplitudes than radial RFs, (2) the direct *P*-wave arrival is close to the predicted travel time for a 1D Earth model and (3) no evidence for large amplitude ringing. The pre-processing used to obtain the receiver functions is similar to the method used by Kahraman et al. (2015), but applied to all three components (vertical, radial, transverse) of the traces in our analysis. To remove the first arrival, which does not contain any additional structural information, we mute the first 2.5 s of each trace following the theoretical *P*-wave arrival.

In total, we use 1396 distinct source-receiver pairs (with 3 components) from 176 events in our analysis. The distribution of sources is shown in Figure 3. Traces were cut and tapered to 100 s and downsampled from the original 50 Hz sampling to 5 Hz. Despite the downsampling, the matrix to invert is very large which limits the achievable resolution and model depth. Typical storage requirements for the matrix inversion using the sparse storage method are ≈ 338 Gb for a model space dimension ($x \times y \times z$) $145 \times 145 \times 118$ km³ with an element size of $5 \times 5 \times 2$ km³ and 1396, 100 s long traces, sampled at 5 Hz. We are able to invert the full dataset without recourse to inverting subsets of data and stacking the resulting images (Frederiksen & Revenaugh, 2004; Zhang & Frederiksen, 2013) leading to improved image quality of our results.

5 RECOVERY TESTS

We tested several 1D background velocity models for data inversion and synthetic data recovery including models by Karahan et al. (2001), Bekler & Gürbüz (2008), and Horasan et al. (2002) and models including constant velocity and linear vertical gradients. The background models are used for raytracing to determine traveltimes of the incident and scattered wavefield. While timing of arrivals changes slightly for all realistic velocity models, the overall recovered structure in our tests does not depend significantly on the choice of background model, although depths of interfaces change due to changes in the traveltimes. We chose to use the model by Karahan et al. (2001) for all inversions presented here (Table 1, Fig. 4). This velocity model is derived from seismic

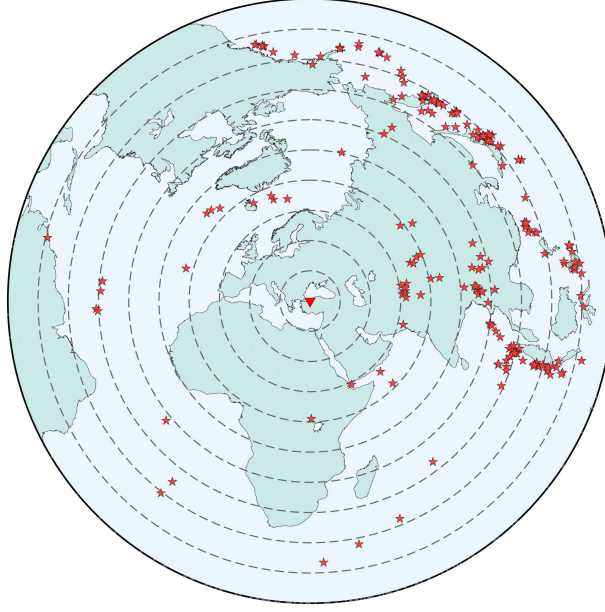


Figure 3. Earthquake locations relative to the center of the DANA array. Dashed circles give distance from DANA center in 10° steps. Earthquakes with $m_b > 5.5$ occurring during the deployment and since 2009 for the permanent stations in an epicentral distance of 30° to 90° were used in the analysis.

324 experiments in the study area and has been used in previous studies using this dataset (Kahraman
325 et al., 2015; Altuncu Poyraz et al., 2015).

326 Figure 5 shows the result of an inversion of the full (1396 individual source-receiver combina-
327 tions) noisy synthetic data generated through the perturbation model (Fig. 4b)). A sub-set of the
328 synthetic traces used in this inversion, i.e. the stations recording event 20123211812 and used in
329 the data inversion, are shown in Fig. 4, c) and d). Synthetic data were generated using ray tracing
330 through the background velocity model with the addition of the scattered wavefield (i.e. the sum-

Depth (km)	V_P (km/s)	V_S (km/s)	ρ (kg/m^3)
0 - 2	3.6	1.967	2.376
2 - 14	5.900	3.225	2.814
14 - 26	6.500	3.552	2.955
26 - 40	7.000	3.691	2.975
\vdots	8.055	4.347	3.326

Table 1. 1D velocity model used in inversion. Depth, P -wave, S -wave and density (ρ) following (Karahan et al., 2001)

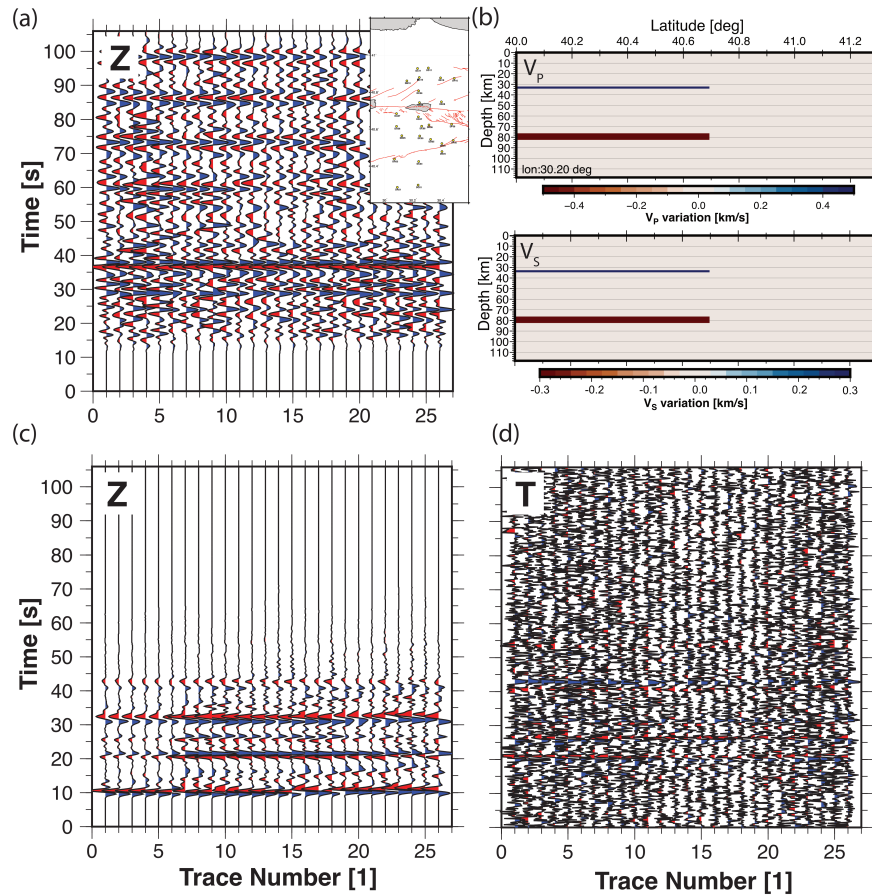


Figure 4. Example data and synthetics. (a) Recorded and deconvolved data example of vertical component of event 20123211812 (insert shows station configuration). Data are cut to 100 s and tapered. The direct P-arrival is suppressed. (b) North-South slices through perturbation model to calculate synthetics. (c) Noiseless synthetics (vertical) through perturbation model shown in b), including all scattering events from direct wave and free surface reflections. Synthetics represent the event-station configuration of the quality-controlled receiver functions for event 20123211812 shown in a). Although the perturbation is not continuous throughout the model, the scattered wavefield can be recorded across the network with distinctive moveout allowing the localisation of the perturbation. (d) Transverse component of the synthetic data calculated for model shown in (b) with added noise. We add Gaussian noise with a 10% standard deviation relative to the maximum signal amplitude to the synthetic data.

331 mation of all contributions of the single scatterers in the model). We use a 0.25 s wide Gaussian
 332 wavelet as the source time function. Synthetic tests use the source-receiver combinations for each
 333 event in the dataset, therefore recreating the same resolution as the recorded dataset. For compari-
 334 son we show the recorded and deconvolved data in Fig. 4a) with the first arrival muted. Scattered
 335 phases can be seen coherently across the traces. The synthetic traces (Fig. 4c,d) show similar struc-

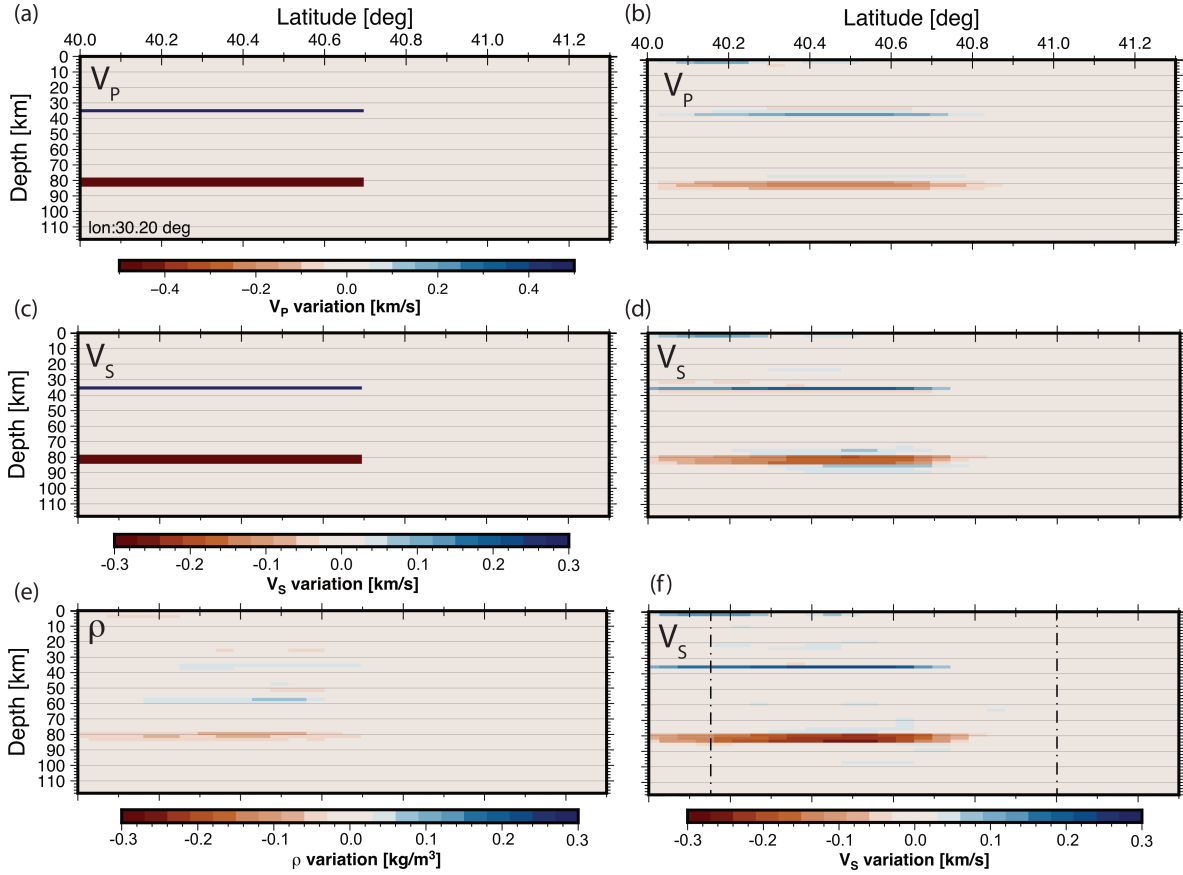


Figure 5. Recovery tests for model shown in Fig. 4 containing heterogeneous V_P and V_S structure. Slices were taken from the 3D model at longitude 30.2° . (a) V_P anomaly of input model containing terminating velocity anomalies at 32 km (negative) and 76 km (positive). Anomaly strength is ± 0.5 km/s. (b) Recovered model after scattering inversion. Due to damping the velocity recovered is smaller than the input model but locations are well resolved. Horizontal smoothing with a standard deviation of a single lateral element (5 km) is applied. (c) as (a) but for V_S . Velocity anomaly is ± 0.3 km/s. (d) As (b) but for V_S . (e) Recovered low amplitude density (ρ) anomaly after inversion. Input model does not contain density variations so recovered anomaly represents cross-talk between the different components. (f) Wiener filtered longitude slice of recovered model to fit recovered depth of anomaly as a zero-phase wavelet. Black dashed lines in f) indicate the perceived limits of the well-resolved region.

336 ture although clearly are not able to capture the full complexity of the data due to the simplicity
 337 of the model (Fig. 4b). Noise is added to the synthetic data through a random number generator
 338 (Marsaglia & Bray, 1964) using 10% RMS amplitude variation Gaussian noise compared to the
 339 direct wave amplitude to produce this noisy synthetic dataset (Fig. 4d).

340 The synthetic model is parameterised with 5 km cell spacing horizontally and 2 km vertically.

341 The model contains a $V_P = +0.5$ km/s and $V_S = +0.3$ km/s anomaly for a single depth element
 342 (2 km) starting at 34 km depth and a $V_P = -0.5$ km/s and $V_S = -0.3$ km/s anomaly with thickness
 343 of 6 km starting at 78 km (Fig. 5 a and c). No density variation was added to the model. The
 344 anomalous layers extend across the model in longitude but terminate 80 km into the model from
 345 the south (approximately at 40.7°N), leaving the part of the model that corresponds to the Istanbul
 346 zone free of a velocity anomaly. The inverted model in Fig. 5 b) and d) shows the recovery of
 347 the input model. Because the inversion uses the Born approximation, which generates signals
 348 from localized perturbation, the recovered model will be a band-pass filtered version of the input.
 349 We apply a Wiener optimum filter to minimize the effects of the inversion process, mainly to
 350 reduce sidelobes to aid interpretation. The optimization filter, as described for example by Gubbins
 351 (2004), is obtained by minimising the residual between the desired output g_t (Fig. 5a,c) and the
 352 signal obtained by convolution of the filter f_t^0 with the actual output x_t (Fig. 5b,d)

$$(e_t)^2 = (g_t - x_t * f_t^0)^2 \quad (10)$$

353 The effect of the inversion and the filter terms acting on a single trace of the synthetic model are
 354 shown in Supplemental Figure S1.

355 Although the input model in this test does not contain any density ($\delta\rho$) heterogeneity, Fig. 5e
 356 shows that the inverted model for the density structure is affected by cross-talk between the differ-
 357 ent parameters (more examples given in Supplemental Figure S2). However, relative amplitudes
 358 $\Delta\rho$ in this model are small and the effect is most prominent in areas with velocity anomalies. Tests
 359 with models including $\Delta\rho$ show that density structure can be resolved. Complete input and output
 360 models for this recovery test and further tests are shown in the Supplemental Figures S2 to S8.

361 These tests show that the recovery of velocity and density anomalies is variable within the
 362 model volume due to the relative sampling of the model volume by the ray configuration of the
 363 dataset. Peripheral regions are generally less well resolved than the center of the volume and areas
 364 of reduced resolution show poor recovery of amplitudes in the inverted model (Fig. 5). Within
 365 the central zone we do not observe strong depth or amplitude variations of the recovered model,
 366 adding confidence to our interpretation. Areas of the model space that are not well resolved are

367 masked in all following figures (and supplemental material) and the approximate limits of the
368 well-resolved volume are shown in the N-S profiles (dot-dashed vertical lines in Fig. 5f), to which
369 we limit our interpretation. These areas are estimated from our recovery tests as shown in Fig. 5
370 and the Supplemental Material.

371 The recovered model in Fig. 5b,d) shows some low-amplitude imaging artefacts around the
372 recovered anomalies but also away from them, which are not fully removed by the Wiener filtering.
373 These are likely due to the sampling of the volume by the dataset as well as the noise added to
374 the synthetic data. Care has been taken when interpreting recorded data inversions to not interpret
375 such artefacts as lithospheric structure.

376 Changing the depth extent of the inverted model space between 48 km and 118 km (in 20 km
377 steps) does not lead to strong changes in the inverted model. A comparison between a 48 km
378 and 118 km deep model containing the same structure for V_P and V_S is shown in supplemental
379 Figure S3 a) and b). This holds even when synthetic traces were generated including structure
380 below the inverted volume (Fig. S3c) showing that heterogeneities underneath the volume are not
381 erroneously mapped into the model volume. In the following section we show models down to
382 depths of 118 km (60 nodes with 2 km spacing) in a trade-off between achievable resolution,
383 model size and required computer memory. The horizontal smoothing leads to some smearing of
384 energy in horizontal directions. Nonetheless, Fig. 5 shows that terminating discontinuities can be
385 accurately located within 1 to 2 horizontal elements (i.e. 5 to 10 km) in the central region of the
386 model space. We also performed recovery tests using other structural models including velocity
387 and density heterogeneities to better understand the performance of the method (for these further
388 recovery tests please see Supplemental Material).

389 **6 RESULTS**

390 The results of the tomographic scattering inversion of the DANA dataset are shown in Fig. 6 and
391 Fig. 7. Fig. 8 presents an interpreted section of the results. Slices in Fig. 6 and 7 were extracted
392 from the three-dimensional inversion volume along North-South (Fig. 6) and East-West (Fig. 7)
393 profiles at locations shown in Fig. 1. The locations of the profiles were chosen to be in similar

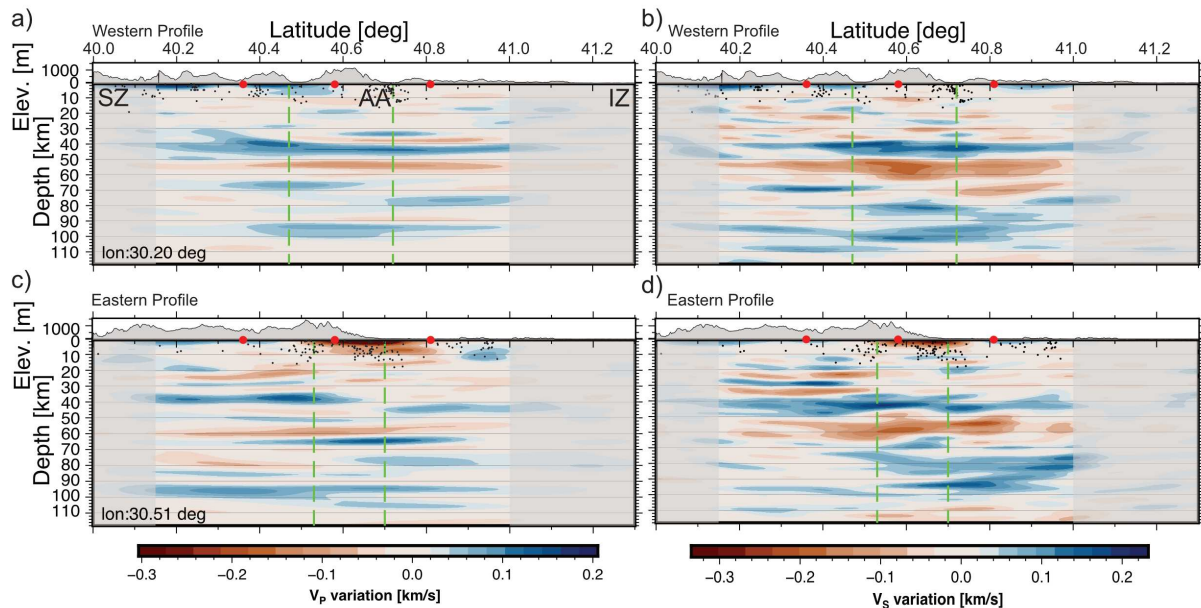


Figure 6. North-south oriented slices along 30.2° (top) and 30.51° (bottom) for the inversion for V_P (left) and V_S (right) structure. Profile locations are indicated in Fig.1. Approximate locations of the southern and northern branches of the NAFZ are shown as dashed green lines. Areas with limited resolution as determined from the recovery tests (Fig. 5) are masked in grey. Red dots indicate locations of EW slices shown in Fig.7. Black circles indicate local seismicity as determined by Altuncu Poyraz et al. (2015) within a ± 5 km corridor projected onto the profile. The top panel in each subpanel shows SRTM topography along the profile (Farr et al., 2007).

394 locations to those shown in Fig. 6 of Kahraman et al. (2015) (for an equivalent display to Kahra-
 395 man et al. (2015) see Supplemental Figure S9 , S11 and S13). Full solutions are presented in the
 396 form of animated GIFs in Figures S15 and S16 of the Supplemental Materials. A *kml* file is also
 397 provided to display the profiles in their correct geographical location. The model is filtered with
 398 the Wiener optimization filter as discussed above. In the following we report depths at the top of a
 399 heterogeneity in the filtered sections which gives the best agreement of input and recovered model
 400 on the recovery tests (e.g. Fig. 5)

401 Generally, the *S*-wave images show greater amplitude and are better constrained. The *S*-wave
 402 tomographic images also seem to show more fine scale structure likely related to the shorter wave-
 403 length. The density ($\Delta\rho$) profiles show some of the major structure and are shown in the supple-
 404 mental Figs. S13 and S15 but suffer from cross-talk as shown in Fig. 5. As the interpretation of

405 the $\Delta\rho$ profiles is more difficult and there is no independent constraint on the density structure we
 406 do not discuss this parameter further in the text.

407 6.1 Western Profile

408 Profiles for V_P (Fig. 6 a) and V_S (Fig. 6 b) have been extracted along a longitude of 30.2° E.
 409 Areas with limited resolution as determined from the recovery tests (Fig. 5) have been masked
 410 in this profile in transparent grey. The V_P profile (Fig. 6a) is dominated by a velocity increase
 411 at ~ 40 km depth for most of the profile, which we associate with the Moho. The Moho velocity
 412 increase bifurcates south of $\sim 40.4^\circ$ with a shallower velocity increase located at ~ 32 km depth
 413 deepening to 40 km at $\sim 40.4^\circ$ N. The anomaly also seems to fade, i.e. showing less of a velocity
 414 anomaly, south of about 40.3° N. The point of bifurcation coincides with the surface expression
 415 of the southern strand of the NAFZ. A similar Moho signal is observed in the S -wave anomaly at
 416 ~ 40 km, shallowing to about 38 km within the Armutlu block, which shows a thickening of this
 417 interface. The S -wave anomaly does not show the same shallow branch observed in the P -waves
 418 but shows lower amplitudes south of $\sim 40.4^\circ$ N, i.e. south of the southern NAFZ strand.

419 Observed crustal structure includes a weak high V_P anomaly at ~ 18 km in the Armutlu block
 420 with weak, complex V_S structure in the Sakarya zone. Complex structure starting at ~ 32 km depth
 421 (positive and negative anomalies) in V_P and V_S can be seen in the vicinity of the northern strand
 422 (40.7° N) just overlying the Moho. The V_P model shows less structure in the upper crust except a
 423 fast anomaly to depths of ~ 5 km around the southern branch and a slow (also seen in V_S) overlying
 424 fast anomaly between ~ 10 km and ~ 20 km depth in the Armutlu block.

425 The high velocity anomaly at 40 km depth is underlain by a strong low V_P and V_S anomaly
 426 at depths of ~ 50 km. This anomaly shows lower amplitudes in the Sakarya Zone with the change
 427 coinciding with the surface expression of the southern NAFZ strand. We also identify a velocity
 428 increase in V_P and V_S at ~ 64 km and ~ 66 km depth, respectively, around 40.4° N (southern
 429 strand) and ~ 74 km in V_P beneath the Istanbul zone (with a termination at the northern strand).
 430 The V_S anomaly shows a low velocity anomaly at ~ 68 km depth just north of the northern strand
 431 changing to a high velocity anomaly at ~ 74 km depth north of 40.9° N.

At greater depths we observe a fast anomaly in V_S at ~ 78 km depth and a fast anomaly in V_P and V_S at ~ 92 km but showing depth variation in V_S . The 78 km anomaly seems to merge with the deeper anomaly in the Istanbul zone.

6.2 Eastern Profile

The eastern North-South profile at 30.51° E (Figs. 6c and 6d) shows more structure, especially in the crust, than the western profile despite the close proximity of the two profiles.

We observe a strong, fast V_P anomaly at a depth of ~ 34 km terminating halfway through the Armutlu block and re-emerging at a depth of ~ 42 km just north of the northern strand in the Istanbul zone. In V_S we observe a more continuous structure with a high velocity anomaly at ~ 36 km depth in the south, stepping to ~ 42 km at $\sim 40.7^\circ$ N coinciding with the northern strand. The V_P anomaly is weak in the Armutlu block on this profile and seems to terminate at 40.6° E, while the V_S anomaly is more continuous, but also weakens in this region. The amplitude variation of these anomalies cannot be explained by the limitations of the sampling (see Fig. 5).

Especially striking in this profile is the complex V_S structure in the Sakarya Zone down to depths of about 30 km manifesting as series of fast and slow anomalies between ~ 10 km and 32 km (see supplemental Figure S7). The V_P structure is similar but weaker than V_S . The structure terminates abruptly at the southern strand with little crustal structure in the Armutlu block. The Adapazari basin (centred at about 40.7° N) is representing as a low velocity anomaly between 40.6° N and 40.7° N to depths of about 6 km (V_S).

Similar to the western profile we identify a slow anomaly in both V_P and V_S at depths of ~ 56 km and ~ 52 km, respectively. The V_S anomaly seems to show more complexity. We identify a weak slow anomaly at ~ 76 km depth in the Sakarya zone in V_P which appears detectable but much weaker in V_S . This anomaly seems to terminate at the southern branch. Fast anomalies are detected at ~ 92 km in V_P and V_S across the profile with shallower fast anomalies for V_P and V_S at ~ 76 km depth beneath the Istanbul zone and the Armutlu block. In V_P there is evidence of this interface splitting into a deeper interface deepening to ~ 102 km across the southern strand.

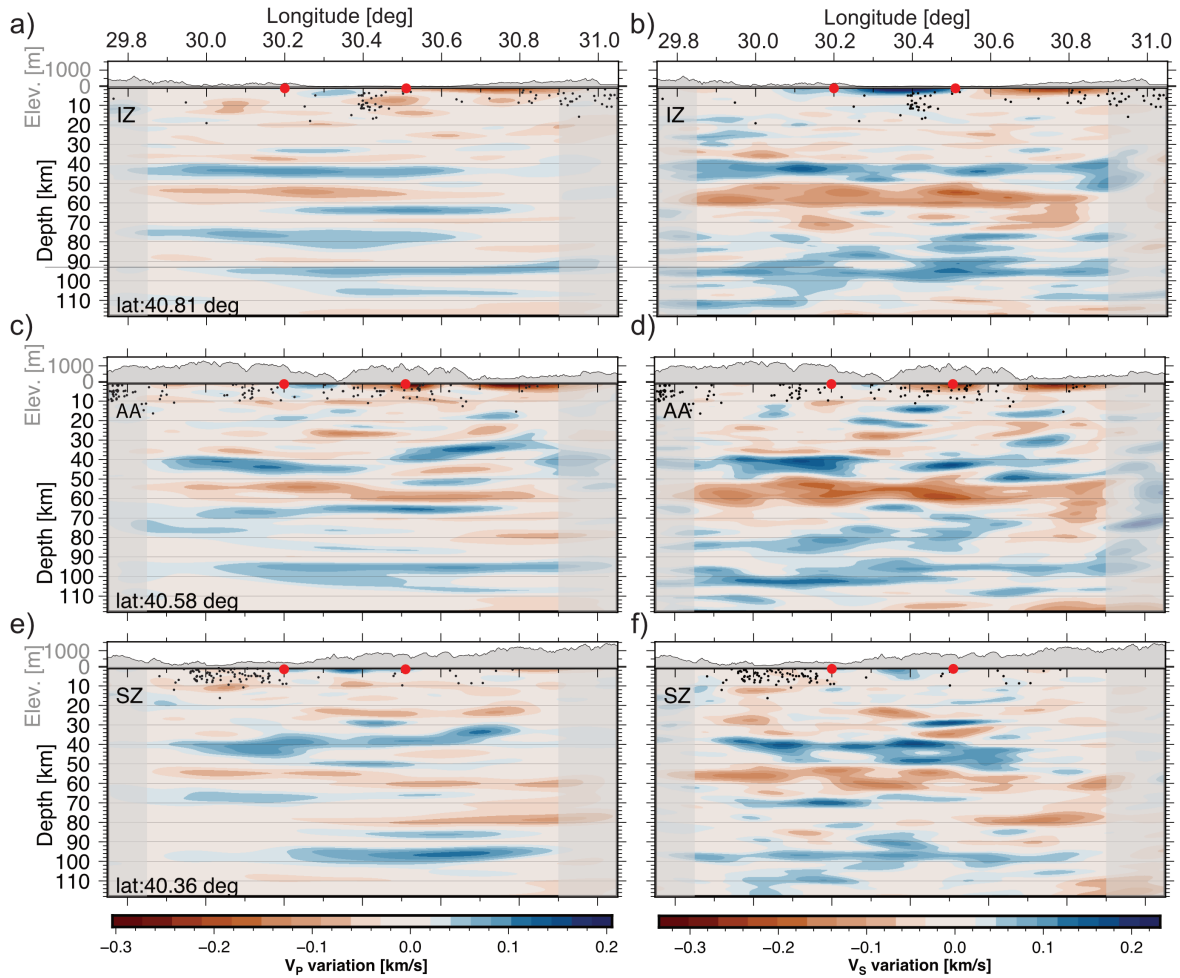


Figure 7. As Fig.6 showing west-east oriented slices through the inverted V_P (left) and V_S (right) structure. Slices are located in the Istanbul zone (IZ - a,b) at latitude 40.81° , the Armutlu-Almacık block (AA - c,d) at 40.58° and Sakarya zone (SZ - e,f) at 40.36° . Areas with limited resolution as determined from the recovery tests (Fig. 5) masked in grey. Black circles indicate local seismicity as determined by Altuncu Poyraz et al. (2015) within a ± 5 km corridor projected onto the profile. The top panel in each subpanel shows SRTM topography along the profile (Farr et al., 2007).

458 6.3 Sakarya Zone

459 The West-East profile for V_P and V_S (Figs. 7e and 7f, respectively) has been extracted along
 460 40.36°N and is fully located within the Sakarya zone. The Sakarya zone is the southernmost
 461 tectonic block in the study region. The inverted scattering tomography model shows a positive
 462 anomaly at depths of ~ 38 km. In V_P this interface shallows to ~ 32 km around 30.6°E . This
 463 anomaly seems rather complex and might be discontinuous. We also identify a laterally limited
 464 fast anomaly at ~ 30 km between 30.4°E and 30.6°E . A deeper slow anomaly at about 54 km

465 depth can be seen that shows a slight step down to about 60 km (V_P) at about 30.4°E and seems
 466 complex in V_S . The western part of the profile shows a fast anomaly at ~68 km, with a slow
 467 anomaly at ~78 km in the east. A fast anomaly at ~98 km depth (94 km in V_P) is identified which
 468 terminates at 30.2°E in V_P .

469 **6.4 Armutlu Block**

470 In contrast to the Sakarya Zone, the Armutlu Block (Figs. 7c and 7d for V_P and V_S , respectively)
 471 shows more structure down to depths of 40 km. A fast anomaly at ~40 km terminates around
 472 30.4°E and appears as shallow as 30 to 32 km further east in V_P . V_S also shows the termination
 473 but a less pronounced step. The step around 30.6° E seems to coincide with the profile moving
 474 from the Armutlu block to the Almacık mountains. West of ~30.4°E, this interface is underlain
 475 by a slow anomaly at ~50 km showing a step to ~58 km at 30.4°E in V_P . Overall V_S seems
 476 more complex. We identify several small scale fast and slow anomalies in the crust, the strongest
 477 at ~14 km around 30.4°E in V_S . Slow anomalies shallower than 40 km are indicated between
 478 30.5°E and 30.9°E.

479 A fast anomaly at ~ 94 km stretches across most of the profile in V_P , with comparable but more
 480 complex structure in V_S . the V_S section also shows more localised structures at depths greater than
 481 80 km.

482 **6.5 Istanbul Zone**

483 The Istanbul zone (Figs. 7a and 7b for V_P and V_S , respectively) shows very little structure down
 484 to depths of about 40 - 42 km where a strong fast anomaly can be detected in V_P and V_S . This
 485 fast anomaly seems to terminate around 30.6°E for V_P but continues across the IZ in V_S . A slow
 486 anomaly is visible in V_S at depths less than 10 km between 30.6°E and 30.9°E and a fast anomaly
 487 between 30.2°E and 30.5°E.

488 The strong Moho signal is underlain by a slow anomaly around 52 km depth again terminating
 489 around 30.6°E for V_P . V_P shows a fast anomaly at ~74 km depth, which like the Moho signal
 490 in this block, terminates at about 30.6.°E; the corresponding structure in V_S is weaker and dis-

491 continuous. A strong fast anomaly at ~ 92 km depth can be seen in V_P and V_S , and again the V_S
492 structure is complex.

493 7 DISCUSSION

494 The scattering tomography results show changes in the structure over distances of 10 km in the
495 lithosphere. The smoothing process implemented in the inversion means that more abrupt changes
496 present in the actual structure would also appear smoothed over that distance. These changes can
497 be related to the different structure of the tectonic blocks (Ben-Zion et al., 2003; Bulut et al.,
498 2012) and manifest in e.g. the North-South profiles but can be detected in the full data volume (see
499 Supplemental Material). Nonetheless, we observe structural changes also in East-West direction
500 similar to those detected earlier (e.g. Barış et al., 2005; Beyhan & Alkan, 2015; Çubuk-Sabuncu
501 et al., 2017) where more continuous structure within the tectonic blocks might be expected

502 The profile across the Armutlu block follows the strike of the NAFZ east of about 30.7°E
503 where it leaves the Armutlu block (Fig. 1). The depth slices through the model shown in Fig. 6 and
504 7 show strong changes between the two north-south trending profiles despite their close proximity.
505 Interpreted NS sections are shown in Fig. 8. We have performed recovery tests for the dominant
506 interpreted structure in the tomographic model (Fig. 9). We include complex crustal structure in
507 the Sakarya zone, a Moho step and lithospheric structure in this complex model. We are able to
508 recover the input structure very well in V_S and V_P with stronger recovered anomaly amplitudes
509 in V_S (Fig. 9a & b). Some low amplitude spurious signals due to noise and the inversion volume
510 sampling are visible in these models as discussed earlier, but are generally of lower amplitude
511 than the recovered model. These are mainly visible close to the input anomalies (Fig. 9 a). The
512 difference in V_P and V_S recovery indicates that a joined interpretation of V_P and V_S might be
513 necessary for robust interpretation of the scattering tomographic images. To highlight the most
514 coherent part of the model we stack the depth profiles in longitude and divide these at 30.4°E to
515 show western and eastern stacks in Fig. 10 for both V_P and V_S . Fig. 11 shows a schematic of the
516 dominant structure in the tomographic images.

517 Comparing the individual slices and the stacked velocity-depth profiles shows that many features

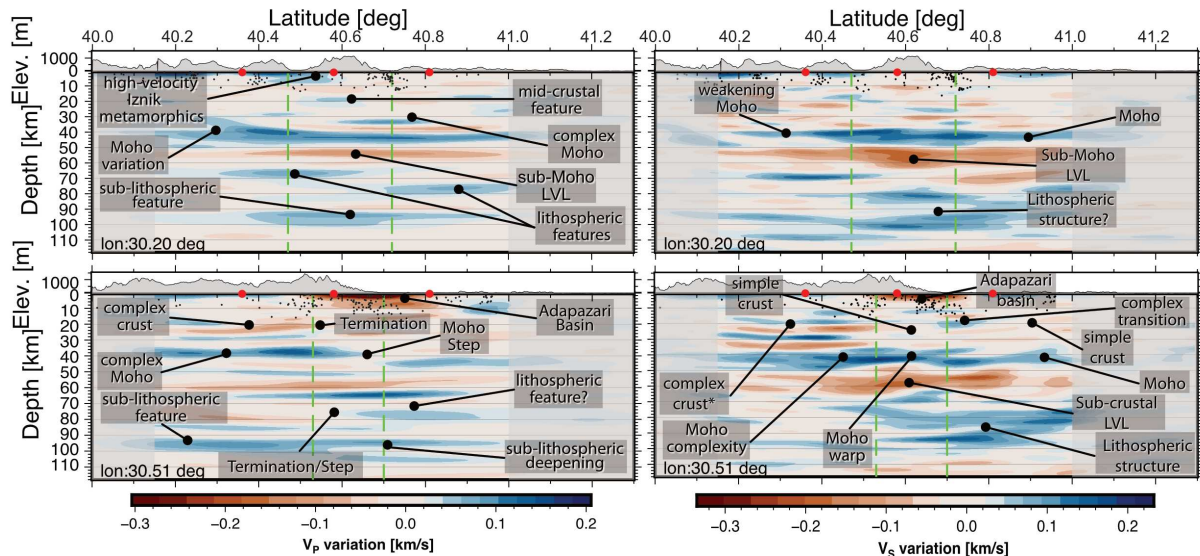


Figure 8. Interpreted NS cross sections for V_P (left) and V_S (right). Shown are North-South oriented slices as in Fig. 6. Black circles indicate local seismicity as determined by Altuncu Poyraz et al. (2015) within a ± 5 km corridor projected onto the profile. The top panel in each subpanel shows SRTM topography along the profile (Farr et al., 2007).

518 are coherent along stretches of the profile, but can change on short scale-lengths in both N-S and
 519 E-W directions.

520 7.1 Mohorovičić discontinuity

521 In the west, the Mohorovičić discontinuity (the Moho) is visible in both V_P and V_S as a dominant
 522 fast velocity at depths of ~ 40 km with variations in V_P in the south and in V_S in the Armutlu
 523 block. In the east the Moho is shallower in the south (34 km (V_P), 38 km (V_S)) but shows a step
 524 to greater depths (42 km) between 40.6° N to 40.7° N at 30.51° E.

525 The deepening of the Moho might indicate the existence of a shear zone at the location of the
 526 northern branch which has also been indicated in teleseismic tomography in this region (Papaleo
 527 et al., 2018, 2017). The Moho at 30.2° E is overlain by a slow anomaly in V_P between 40.7° N and
 528 40.9° N (Fig. 8). In the V_S model there is weak evidence for a similar, but weak and intermittent,
 529 structure between 40.8 and 41.0° N.

530 In the east, the Moho seems much weaker and discontinuous across all three tectonic blocks.
 531 The strongest change in Moho depth can be identified around 40.8° N in the eastern profile where

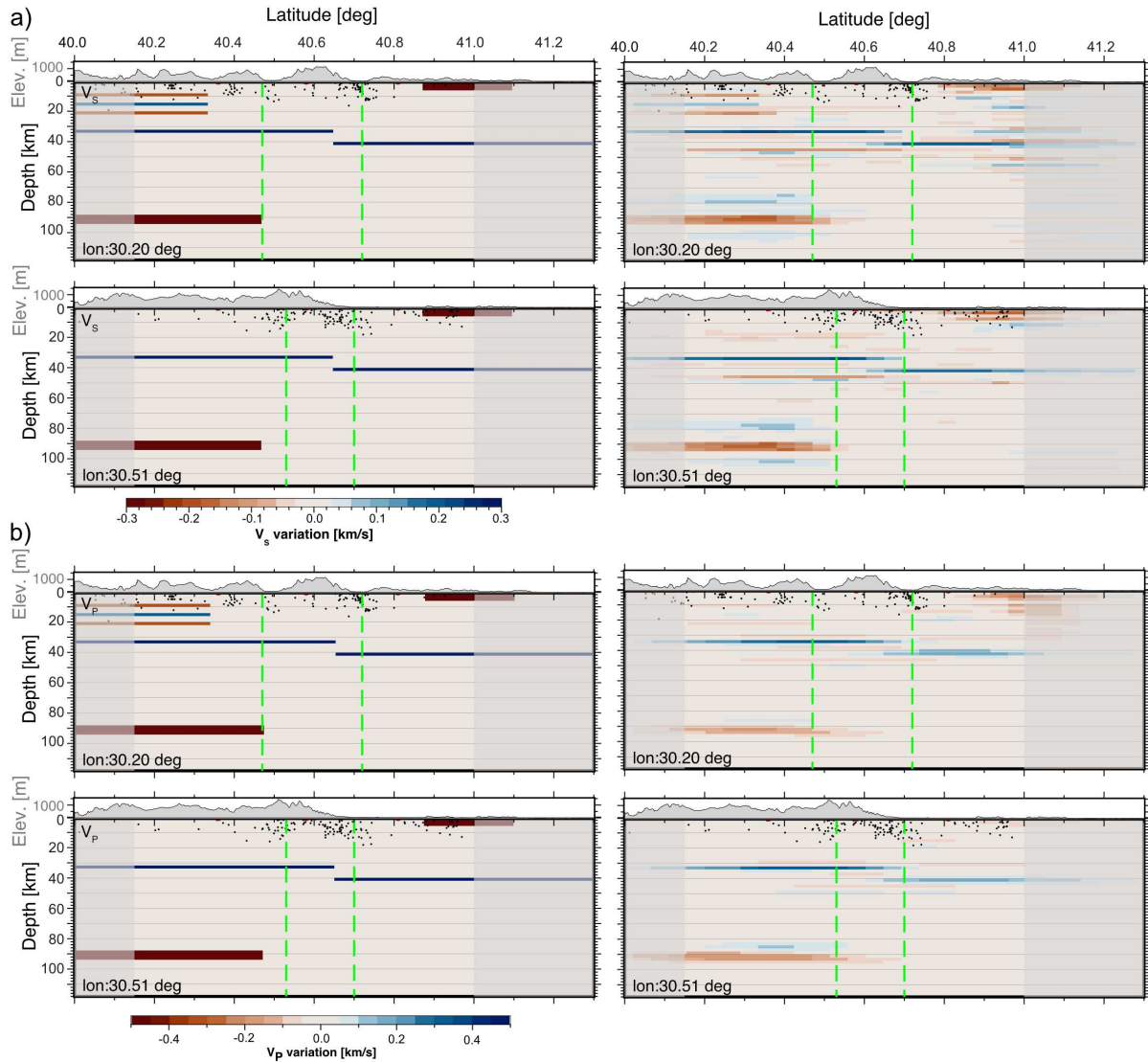


Figure 9. Recovery test for complex synthetic model containing V_P and V_S anomalies in the crust, a stepped Moho like structure and a deeper low velocity anomaly. This model is similar to the dominant structures interpreted in the discussion. a) V_S structure along NS profiles along 30.2° E (top) and 30.51° E (bottom). The input model is shown on the left, the recovered model on the right. b) as a) but for V_P .

532 we observe a step from 32 km to 40 km coinciding with the surface expression of the northern
 533 branch. For the northern branch the discontinuous structure seems to extend into the mantle as
 534 discussed later.

535 While there are strong north-south changes in the profiles in Figs. 6 to 10 we also observe
 536 strong east-west changes, e.g. in the Sakarya zone with a complex Moho structure around 30.5° E
 537 and the weakening of the Moho east of 30.4° E or the change in the Armutlu block at $\sim 30.5^\circ$ E. The
 538 latter might be related to the step-over structure of the NAFZ related to the differential movement

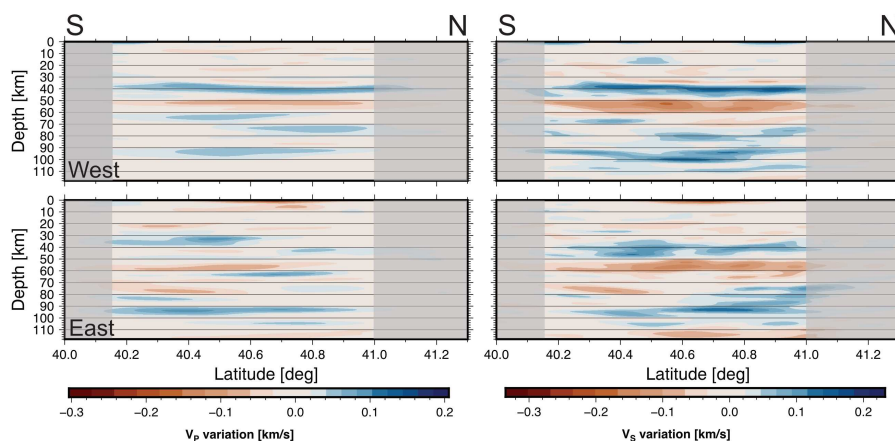


Figure 10. North-South depth slices of the model stacked in longitude (a) for dV_P and (b) dV_S . Top figure for each velocity variation is for the western section (west of 30.4° E) of the model with the bottom the eastern part (east of 30.4° E).

539 of the Armutlu and Almacık blocks and the trend of the suture zones between the tectonic blocks.
 540 We also observe a pronounced change of the Moho depth between the Armutlu block and the
 541 Almacık mountains at around 30.6° E (Suppl. Fig. S14, S15), indicating strong contrasts in crustal
 542 structure from the Armutlu block to the SNAFZ shear zone.

543 7.2 Crustal structure

544 We find evidence for strong crustal structure variation along some of the profiles. The most striking
 545 structure is the apparent strong crustal layering south of the southern branch in the Sakarya zone
 546 (Fig. 6 c,d) for both V_P and V_S (best visible in V_S). The crustal heterogeneity is clearly truncated
 547 by the surface location of the southern branch and forward models indicate that it consists of a
 548 series of high and low velocity anomalies (e.g. Fig. 9) perhaps related to emplacement of magmatic
 549 sills during the Tethys closure (Karabulut et al., 2003). The crust in the Armutlu block on the other
 550 hand is relatively homogeneous, adding to the stark difference across the southern NAFZ branch.

551 Overlying the Moho in the area of the northern strand along the eastern profiles we detect
 552 small-scale, complex Moho structure. Modeling indicates that it could be related to a heterogeneity
 553 with limited extent approximating a point scatterer perhaps related to the material property changes
 554 in the fault zone. The lateral smoothing inherent to our inversions leads to a lack of resolution in
 555 this case.

556 We detect evidence for the Adapazari basin as low velocity anomalies between 40.6°N and
 557 40.8°N in the eastern profiles. Our method does not allow the necessary depth resolution at these
 558 depths for conclusion on the depth of the basin. The high velocity Iznik metamorphics (Taylor
 559 et al., 2019a) can be detected between 40.4°N and 40.6°N in the western profile.

560 Areas in the proximity of the surface expressions of the northern and southern strands show
 561 more heterogeneous structures than areas further away, perhaps related to increased damage around
 562 the fault zone (Ben-Zion & Sammis, 2003). We detect a few localized crustal heterogeneities in the
 563 Sakarya zone and Armutlu block. There is evidence for a more continuous low velocity anomaly
 564 at ~ 10 km and ~ 25 km depth in the Armutlu block and the Sakarya zone that is best visible in
 565 the V_P models (Fig. 7). The scattering tomography shows less heterogeneity in the Istanbul Zone
 566 than in the neighboring tectonic units of the Armutlu block and the Sakarya Zone, which could be
 567 related to the reported absence of metamorphism and the lack of major deformation (Okay, 1989).

568 7.3 Sub-crustal structure

569 Below the Moho we identify a dominant low velocity layer at depths between ~ 50 and ~ 60 km
 570 in the north-south profiles for V_P and V_S (Fig. 10). The low velocity layer weakens but remains
 571 observable around 40.6°N and is possibly linked to the surface expression of the northern strand.
 572 The weakening is more pronounced in V_P than V_S . The interface to the anomaly is slightly deeper
 573 (52 km) in the stacked eastern profile but also shows changes in the extent of the reduced seismic
 574 velocities from travelttime tomography (Papaleo et al., 2017, 2018). The continuity of this structure
 575 beneath all tectonic blocks, although with possible depth and structural variations, indicates that
 576 it is related to lithospheric structure post-dating the amalgamation of northern Anatolia and the
 577 development of the suture zones. It is similar to a signal detected by Kahraman et al. (2015).

578 The fast anomalies detected at depths greater than 60 km show changes in depth and structure
 579 in the vicinity of the surface locations of the NAFZ branches although slightly offset to the north,
 580 possibly consistent with shear zones that dip to the North (Kahraman et al., 2015; Papaleo et al.,
 581 2017, 2018). The tectonic implications of such a northerly dip remain unclear.

582 There is little evidence for a coherent deep low velocity anomaly in our model that can be

583 interpreted as a Lithosphere-Asthenosphere boundary (LAB). The lower part of the models seems
584 dominated by high velocity anomalies, although there is weak evidence for a low velocity anomaly
585 in V_S between 110 and 120 km depth. Results from previous studies suggesting shallow LAB
586 depths between 80 and 100 km are confirmed in the entire region outside the subduction zones
587 (Kind et al., 2015). Therefore we cannot confirm a detection of the LAB in our models. The LAB
588 might be too gradational to show up as signal in the P -wave coda and to be imaged using our
589 method.

590 **7.4 Shear zones**

591 In our scattering tomographic model we see the strongest evidence for the NAFZ shear zone in the
592 abrupt changes of crustal and sub-crustal structures. We see crustal structures that terminate on or
593 near both fault strands, most clearly in the changes of the crustal structure transitioning from the
594 Sakarya Zone to the Armutlu block (i.e. across the SNAFZ) which we can trace to Moho depths
595 (e.g. Fig. 6c,d). In general, the AA shows almost no heterogeneity in the crust. At the northern
596 boundary of the AA, coinciding with the NNAFZ we detect energy that seems consistent with the
597 existence of a laterally very limited heterogeneity (Fig 8) that might be related to the damage zone
598 of the fault zone (Ben-Zion & Sammis, 2003).

599 The Moho step detected in the eastern profiles (e.g. Fig 6c, d)) seems to coincide with the
600 surface expression of the NNAFZ and might indicate a localized subvertical shear zone extending
601 deeper than the Moho and into the mantle. Some interfaces in the lithospheric mantle (e.g. Fig
602 6a,c) also show terminations coinciding with the NNAFZ indicating sub-Moho structure related to
603 the shear zone. Willis et al. (2019) showed that localization of a shear zone in the lower crust can
604 be produced by thermal activation in this tectonic setting if the crust has a rheology comparable to
605 that of dry plagioclase. Furthermore, thermally activated shear zone localization of the upper 10
606 km or so of the mantle is also possible for a dry peridotite rheology.

607 Other continental transform faults such as the San Andreas Fault system (SAF), the Alpine
608 Fault (AF) and the Dead Sea Transform (DST) show similar structures (e.g Stern & McBride,
609 1998; Weber et al., 2004; Mohsen et al., 2005; Ford et al., 2014) indicating localized shear through-

610 out the crust . The SAF in southern California (Yan & Clayton, 2007) and the DST along the Aravia
611 fault (Mohsen et al., 2005) seem to offset the Moho in close proximity to the surface expression
612 of the fault similar to the eastern profiles across the NAFZ. There is evidence that the SAF also
613 offsets the LAB even in the upper mantle (Ford et al., 2014).

614 Due to the intra-Pontide suture zone that juxtaposes tectonic blocks of different provenance in
615 the study area, it is difficult to separate the residual signature of a suture zone from the shear zone.
616 The NAFZ seems to exploit a crust weakened by the presence of sutures. Nonetheless, our results
617 provide first evidence that the southern branch might extend throughout the crust (Fig. 6). We also
618 see evidence in the crust indicating small-scale heterogeneity coinciding with the location of the
619 southern and northern strands .

620 **7.5 Comparison to receiver function structure**

621 Our results allow a comparison with crust and upper mantle structures resolved in the region using
622 other approaches. Direct comparison with the *P*-wave receiver function study of (Kahraman et al.,
623 2015) using the same receiver array combines the comparative strength of scattering tomography
624 in imaging lateral and vertical changes with the receiver function sensitivity to vertical disconti-
625 nities. Kahraman et al. (2015) noted pronounced variations in crust and upper mantle structure
626 and properties both in north-south and east-west directions in agreement with this and other stud-
627 ies (e.g. Çubuk-Sabuncu et al., 2017; Beyhan & Alkan, 2015). Kahraman et al. (2015) imaged
628 lateral terminations in key sub-horizontal discontinuities beneath the southern and northern fault
629 zones. Here we constrain: 1) complex crustal layering in the Sakarya zone towards the east; and
630 2) a mid-crustal feature in the Armutlu block in the west of the study region, which appears to be
631 confined by NAFZ fault branches extending deeper into the crust. Kahraman et al. (2015) find a
632 deepening of the Moho from north to south in the east which is not as clearly seen in this study
633 and they do not show evidence for a step in Moho depth roughly along the surface expression of
634 the northern NAFZ, although there is a high-amplitude receiver function signal beneath the Moho
635 in the Istanbul Zone, which may indicate a sub-crustal anomaly. Kahraman et al. (2015) show
636 evidence for structure in the lithospheric mantle in some parts of their profiles that is broadly in

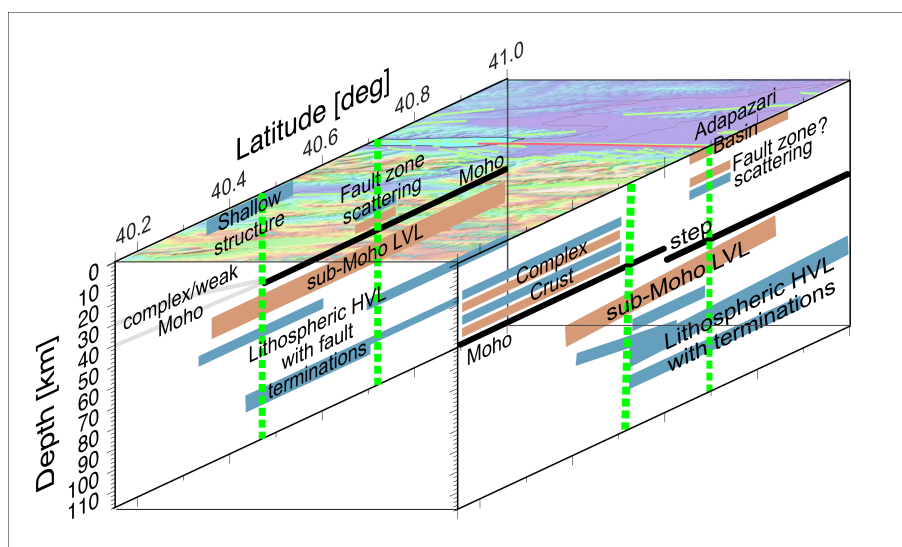


Figure 11. Cartoon of the dominant structures identified in the scattering tomography. We detect crustal and mantle lithospheric structure as well as the crust-mantle interface which all seem to be affected by the North-Anatolian Fault Zone. Top shows shuttle radar topography (SRTM) from Farr et al. (2007).

637 agreement with structures resolved in this study. In particular, their anomaly at ~ 60 km depth
 638 beneath the Istanbul Zone is co-located with a sub-Moho low-velocity zone seen here (Fig. 8). A
 639 northwards dipping shear zone, interpreted through the termination of interfaces in the crust and
 640 lithospheric mantle in Kahraman et al. (2015), is not evident in the scattering tomography results.
 641 Instead, we observe a Moho step beneath the northern NAFZ surface expression and terminations
 642 of lithospheric features beneath the NNAFZ could indicate a sub-vertical extension of the fault
 643 zone into the lithospheric mantle. In contrast, the SNAFZ appears to terminate at the Moho in the
 644 scattering tomography results, in agreement with Kahraman et al. (2015).

645 8 CONCLUSION

646 We have used data from a dense deployment of seismometers over the actively deforming North
 647 Anatolian Fault Zone in the region of the 1999 İzmit and Düzce ruptures to analyse the scattered
 648 seismic wavefield following teleseismic P -wave arrivals. Extending the analysis of the scattered
 649 seismic wavefield to a tomographic inversion (Frederiksen & Revenaugh, 2004) we detect crustal
 650 and mantle heterogeneities that can be linked to the structure and tectonics of the lithosphere
 651 beneath the North Anatolian Fault Zone in north-west Turkey. Our high-resolution images from the

652 scattering tomography down to depths of 120 km allow unprecedented insight into the lithospheric-
653 scale structure of a major continental strike-slip fault. We show complex structure in crust and
654 lithospheric mantle that can be linked to modern active tectonic processes as well as the structure
655 of the crustal terranes that form the region (Fig. 11).

656 Our tomographic models show complex crustal structure in the Sakarya zone terminating at
657 the southern branch of the NAFZ and terminations of crustal discontinuities at the northern branch.
658 The terminations of crustal structure are sharp within the resolution of our approach. We observe
659 a step in Moho depth coinciding with the surface location of the northern branch of the NAFZ
660 across most of the study region. Terminations of sub-horizontal structures beneath the Moho might
661 indicate that the shear zone extends into the upper mantle to depths of at least 75 km. We detect
662 changes in lithospheric structure perpendicular and parallel to the NAFZ indicating the imprint of
663 complex tectonic history of the region onto the lithospheric structure.

664 We show that scattering tomography in conjunction with dense recordings of the seismic wave-
665 field is able to provide deeper insight into crustal and mantle structure and the fine-scale structure
666 around fault zones adding to our knowledge of lithospheric structure around fault zones. Strain
667 associated with the NAFZ seems to be localized through the crust and into the mantle. The NAFZ
668 likely exploits weaknesses due to old sutures in this region following the northwards subduction
669 of the Tethys during the amalgamation of Anatolia.

670 **ACKNOWLEDGMENTS**

671 DANA (Dense Array for Northern Anatolia) is part of the FaultLab project (DANA, 2012), a
672 collaborative effort by the University of Leeds, Boğaziçi University Kandilli Observatory and
673 Earthquake Research Institute (BU-KOERI) and Sakarya University. Major funding was provided
674 by the UK Natural Environment Research Council (NERC) under grant NE/I028017/1. Equip-
675 ment was provided and supported by the NERC Geophysical Equipment Facility (SEIS-UK) Loan
676 947. This project is also supported by Boğaziçi University Scientific Research Projects (BAP) un-
677 der grant 6922 and Turkish State Planning Organisation (DPT) under the TAM project, number
678 2007K120610. COMET is the NERC Centre for the Observation and Modelling of Earthquakes,

679 Volcanoes and Tectonics, a partnership between UK Universities and the British Geological Sur-
680 vey. We thank two anonymous reviewers and editor Huajian Yao for comments.

681 **9 DATA AVAILABILITY**

682 All data for this study (DANA, 2012) are freely available from the IRIS DMS under the network
683 code YK. More information on the data can be found under the data DOI doi:10.7914/SN/YH_
684 2012. <http://ds.iris.edu/gmap/YH?timewindow=2012/5/01-2013/10/01>

685 **References**

- 686 Akbayram, K., Sorlien, C. C., & Okay, A. I., 2016. A minimum 52 ± 1 km of total offset along
687 the northern branch of the North Anatolian Fault in northwest Turkey, *Tectonophysics*, **668 -**
688 **669**, 35 – 41.
- 689 Aki, K. & Richards, P. G., 2002. *Quantitative Seismology*, University Science Books.
- 690 Altuncu Poyraz, S., Teoman, M., Türkelli, N., Kahraman, M., Cambaz, D., Mutlu, A., Rost, S.,
691 Houseman, G., Thompson, D., Cornwell, D., Utkucu, M., & Gülen, L., 2015. New constraints
692 on micro-seismicity and stress state in the western part of the North Anatolian Fault Zone:
693 Observations from a dense seismic array, *Tectonophysics*, **656**, 190–201.
- 694 Bakırcı, T., Yoshizawa, K., & Özer, M. F., 2012. Three-dimensional S-wave structure of the upper
695 mantle beneath Turkey from surface wave tomography, *Geophysical Journal International*, pp.
696 1058–1076.
- 697 Barış, S., Nakajima, J., Hasegawa, A., Honkura, Y., Ito, A., & Balamir, S., 2005. Three-
698 dimensional structure of V_p , V_s and V_p/V_s in the upper crust of the Marmara region, NW
699 Turkey, *Earth, Planets and Space*, **57**(11), 1019–1038.
- 700 Barka, A., 1992. The North Anatolian Fault Zone, *Annales tectonicae*, **Vol. 6**, 164–195.
- 701 Barka, A., Akyüz, H. S., Altunel, E., Sunal, G., Çakır, Z., Dikbas, A., Yerli, B., Armijo, R., Meyer,
702 B., de Chabaliér, J. B., Rockwell, T., Dolan, J. R., Hartleb, R., Dawson, T., Christofferson, S.,
703 Tucker, A., Fumal, T., Langridge, R., Stenner, H., Lettis, W., Bachhuber, J., & Page, W., 2002.

- 704 The surface rupture and slip distribution of the 17 August 1999 İzmit earthquake (M7.4), North
705 Anatolian Fault, *Bulletin of the Seismological Society of America*, **92**(1), 43–60.
- 706 Bekler, T. & Gürbüz, C., 2008. Insight into the crustal structure of the Eastern Marmara Region,
707 NW Turkey, *Pure and Applied Geophysics*, **165**(2), 295–309.
- 708 Ben-Zion, Y. & Sammis, C. G., 2003. Characterization of fault zones, *Pure and Applied Geo-*
709 *physics*, **160**(3-4), 677–715.
- 710 Ben-Zion, Y., Peng, Z., Okaya, D., Seeber, L., Armbruster, J. G., Ozer, N., Michael, A. J., Baris,
711 S., & Aktar, M., 2003. A shallow fault-zone structure illuminated by trapped waves in the
712 Karadere-Düzce branch of the North Anatolian Fault, western Turkey, *Geophysical Journal*
713 *International*, **152**(3), 699–717.
- 714 Berk Biryol, C., Beck, S. L., Zandt, G., & Özacar, A. A., 2011. Segmented African lithosphere
715 beneath the Anatolian region inferred from teleseismic P-wave tomography, *Geophysical Jour-*
716 *nal International*, **184**(3), 1037–1057.
- 717 Beyhan, G. & Alkan, M. A., 2015. Three-dimensional structure of Vp in the upper crust of the
718 Sakarya Basin, NW Turkey, *Arabian Journal of Geosciences*, **8**(8), 6371–6383.
- 719 Biryol, C. B., Zandt, G., Beck, S. L., Ozacar, A. A., Adiyaman, H. E., & Gans, C. R., 2010. Shear
720 wave splitting along a nascent plate boundary: the North Anatolian Fault Zone, *Geophysical*
721 *Journal International*, **181**(3), 1201–1213.
- 722 Blom, N., Gokhberg, A., & Fichtner, A., 2020. Seismic waveform tomography of the central and
723 eastern Mediterranean upper mantle, *Solid Earth*, **11**(2), 669–690.
- 724 Bostock, M. & Rondenay, S., 1999. Migration of scattered teleseismic body waves, *Geophysical*
725 *Journal International*, **137**(3), 732–746.
- 726 Bulut, F., Ben-Zion, Y., & Bohnhoff, M., 2012. Evidence for a bimaterial interface along the
727 Mudurnu segment of the North Anatolian Fault Zone from polarization analysis of P waves,
728 *Earth and Planetary Science Letters*, **327-328**, 17–22.
- 729 Bürgmann, R. & Dresen, G., 2008. Rheology of the Lower Crust and Upper Mantle: Evidence
730 from Rock Mechanics, Geodesy, and Field Observations, *Annual Review of Earth and Planetary*
731 *Sciences*, **36**(1), 531–567.

- 732 Çubuk-Sabuncu, Y., Taymaz, T., & Fichtner, A., 2017. 3-D crustal velocity structure of west-
733 ern Turkey: Constraints from full-waveform tomography, *Physics of the Earth and Planetary*
734 *Interiors*, **270**, 90–112.
- 735 DANA, 2012. Dense Array for North Anatolia (DANA), International Federation of Digital
736 Seismograph Networks, doi: 10.7914/SN/YH_2012.
- 737 Dueker, K. G. & Sheehan, A. F., 1997. Mantle discontinuity structure from midpoint stacks of
738 converted P to S waves across the Yellowstone hotspot track, *Journal of Geophysical Research:*
739 *Solid Earth*, **102**(B4), 8313–8327.
- 740 Emre, Ö., Duman, T. Y., Özalp, S., Şaroğlu, F., Olgun, Ş., Elmacı, H., & Çan, T., 2018. Active
741 fault database of Turkey, *Bulletin of Earthquake Engineering*, **16**(8), 3229–3275.
- 742 England, P., G., H., & J.-M., N., 2016. Constraints from GPS measurements on the dynamics of
743 deformation in Anatolia and the Aegean, *Journal of Geophysical Research*, **121**, 8888–8916.
- 744 Farr, T. G., Rosen, P. A., Caro, E., Crippen, R., Duren, R., Hensley, S., Kobrick, M., Paller,
745 M., Rodriguez, E., Roth, L., Seal, D., Shaffer, S., Shimada, J., Umland, J., Werner, M., Oskin,
746 M., Burbank, D., & Alsdorf, D., 2007. The Shuttle Radar Topography Mission, *Reviews of*
747 *Geophysics*, **45**(2), RG2004.
- 748 Fichtner, A., Saygin, E., Taymaz, T., Cupillard, P., Capdeville, Y., & Trampert, J., 2013. The
749 deep structure of the North Anatolian Fault Zone, *Earth and Planetary Science Letters*, **373**,
750 109–117.
- 751 Flerit, F., Armijo, R., King, G. C., Meyer, B., & Barka, A., 2003. Slip partitioning in the Sea of
752 Marmara pull-apart determined from GPS velocity vectors, *Geophysical Journal International*,
753 **154**(1), 1–7.
- 754 Ford, H. A., Fischer, K. M., & Lekic, V., 2014. Localized shear in the deep lithosphere beneath
755 the san andreas fault system, *Geology*, **42**(4), 295–298.
- 756 Frederiksen, A. & Revenaugh, J., 2004. Lithospheric imaging via teleseismic scattering tomog-
757 raphy, *Geophysical Journal International*, **159**(3), 978–990.
- 758 Frederiksen, A. W., Thompson, D. A., Rost, S., Cornwell, D. G., Gülen, L., Houseman, G. A.,
759 Kahraman, M., Poyraz, S. A., Teoman, U. M., Türkelli, N., & Utkucu, M., 2015. Crustal thick-

- 760 ness variations and isostatic disequilibrium across the North Anatolian Fault, western Turkey,
761 *Geophysical Research Letters*, **42**(3), 751–757.
- 762 Govers, R. & Fichtner, A., 2016. Signature of slab fragmentation beneath Anatolia from full-
763 waveform tomography, *Earth and Planetary Science Letters*, **450**, 10–19.
- 764 Gubbins, D., 2004. *Time Series Analysis and Inverse Theory for Geophysicists*, Cambridge Uni-
765 versity Press.
- 766 Gülen, L., 2002. Surface Fault Breaks, Aftershock Distribution, and Rupture Process of the 17
767 August 1999 İzmit, Turkey, Earthquake, *Bulletin of the Seismological Society of America*, **92**(1),
768 230–244.
- 769 Horasan, G., Gülen, L., Pinar, A., Kalafat, D., Özel, N., Kuleli, H. S., & Isikara, A. M., 2002.
770 Lithospheric structure of the Marmara and Aegean regions, Western Turkey, *Bulletin of the*
771 *Seismological Society of America*, **92**(1), 322–329.
- 772 Hurd, O. & Bohnhoff, M., 2012. Stress- and structure-induced shear-wave anisotropy along the
773 1999 İzmit rupture, Northwest Turkey, *Bulletin of the Seismological Society of America*, **102**(5),
774 2177–2188.
- 775 Hussain, E., Hooper, A., Wright, T. J., Walters, R. J., & Bekaert, D. P. S., 2016. Interseismic
776 strain accumulation across the central North Anatolian Fault from iteratively unwrapped InSAR
777 measurements, *Journal of Geophysical Research: Solid Earth*, **121**(12), 9000–9019.
- 778 Jenkins, J., Stephenson, S. N., Martínez-Garzón, P., Bohnhoff, M., & Nurlu, M., 2020. Crustal
779 Thickness Variation Across the Sea of Marmara Region, NW Turkey: A Reflection of Modern
780 and Ancient Tectonic Processes, *Tectonics*, **39**(7).
- 781 Ji, Y. & Nataf, H.-C., 1998. Detection of mantle plumes in the lower mantle by diffraction
782 tomography: theory, *Earth and Planetary Science Letters*, **159**(3-4), 87–98.
- 783 Kahraman, M., Cornwell, D., Thompson, D., Rost, S., Houseman, G., Türkelli, N., Teoman, U.,
784 Altuncu Poyraz, S., Utkucu, M., & Gülen, L., 2015. Crustal-scale shear zones and heteroge-
785 neous structure beneath the North Anatolian Fault Zone, Turkey, revealed by a high-density
786 seismometer array, *Earth and Planetary Science Letters*, **430**.
- 787 Karabulut, H., Özalaybey, S., Taymaz, T., Aktar, M., Selvi, O., & Kocaoğlu, A., 2003. A tomo-

- 788 graphic image of the shallow crustal structure in the Eastern Marmara, *Geophysical Research*
789 *Letters*, **30**(24).
- 790 Karahan, A. E., Karahan, A. E., Berckhemer, H., & Baier, B., 2001. Crustal structure at the west-
791 ern end of the North Anatolian Fault Zone from deep seismic sounding, *Annals of Geophysics*,
792 **44**(1).
- 793 Kind, R., Eken, T., Tilmann, F., Sodoudi, F., Taymaz, T., Bulut, F., Yuan, X., Can, B., & Schnei-
794 der, F., 2015. Thickness of the lithosphere beneath Turkey and surroundings from S-receiver
795 functions, *Solid Earth*, **6**(3), 971–984.
- 796 Koulakov, I., Bindi, D., Parolai, S., Grosser, H., & Milkereit, C., 2010. Distribution of Seismic
797 Velocities and Attenuation in the Crust beneath the North Anatolian Fault (Turkey) from Local
798 Earthquake Tomography, *Bulletin of the Seismological Society of America*, **100**(1), 207–224.
- 799 Langston, C. A., 1979. Structure under Mount Rainier, Washington, inferred from teleseismic
800 body waves, *Journal of Geophysical Research*, **84**(B9), 4749.
- 801 Legendre, C. P., Zhao, L., & Tseng, T.-L., 2021. Large-scale variation in seismic anisotropy in
802 the crust and upper mantle beneath Anatolia, Turkey, *Communications Earth & Environment*,
803 **2**(1), 73.
- 804 Lemnifi, A. A., Elshaafi, A., Karaoğlu, Ö., Salah, M. K., Aouad, N., Reed, C. A., & Yu, Y., 2017.
805 Complex seismic anisotropy and mantle dynamics beneath Turkey, *Journal of Geodynamics*,
806 **112**, 31–45.
- 807 Li, Z., Zhang, H., & Peng, Z., 2014. Structure-controlled seismic anisotropy along the Karadere-
808 Düzce branch of the North Anatolian Fault revealed by shear-wave splitting tomography, *Earth*
809 *and Planetary Science Letters*, **391**, 319–326.
- 810 Ligorria, J. P. & Ammon, C. J., 1999. Iterative deconvolution and receiver function estimation,
811 *Bulletin of the Seismological Society of America*, **89**(October), 1395–1400.
- 812 Marsaglia, G. & Bray, T., 1964. A convenient method for generating normal variable, *Siam*
813 *Review*, **6**, 260–264.
- 814 McKenzie, D., 1972. Active Tectonics of the Mediterranean Region, *Geophysical Journal Inter-*
815 *national*, **30**(2), 109–185.

- 816 Meade, B. J., Hager, B. H., McClusky, S. C., Reilinger, R. E., Ergintav, S., Lenk, O., Barka, A., &
817 Özener, H., 2002. Estimates of seismic potential in the Marmara Sea region from block models
818 of secular deformation constrained by global positioning system measurements, *Bulletin of the*
819 *Seismological Society of America*, **92**(1), 208–215.
- 820 Mohsen, A., Hofstetter, R., Bock, G., Kind, R., Weber, M., Wylegalla, K., & Rumpker, G., 2005.
821 A receiver function study across the Dead Sea Transform, *Geophysical Journal International*,
822 **160**(3), 948–960.
- 823 Moore, J. D. & Parsons, B., 2015. Scaling of viscous shear zones with depth-dependent viscosity
824 and power-law stress-strain-rate dependence, *Geophysical Journal International*, **202**(1), 242–
825 260.
- 826 Najdahmadi, B., Bohnhoff, M., & Ben-Zion, Y., 2016. Bimaterial interfaces at the Karadere
827 segment of the North Anatolian Fault, northwestern Turkey, *Journal of Geophysical Research*,
828 **121**(2), 931–950.
- 829 Okay, A., 1989. *Tectonic Evolution of the Tethyan Region*, chap. Tectonic Units and Sutures in
830 the Pontides, Northern Turkey, pp. 109–116, Springer.
- 831 Okay, A. I., Bozkurt, E., Satir, M., Yiğitbaş, E., Crowley, Q. G., & Shang, C. K., 2008. Defining
832 the southern margin of Avalonia in the Pontides: Geochronological data from the Late Protero-
833 zoic and Ordovician granitoids from NW Turkey, *Tectonophysics*, **461**(1-4), 252–264.
- 834 Paige, C. C. & Saunders, M. A., 1982. LSQR: An algorithm for sparse linear equations and
835 sparse least squares, *ACM Trans. Math. Software*, pp. 43–71.
- 836 Papaleo, E., Cornwell, D. G., & Rawlinson, N., 2017. Seismic tomography of the North Anatolian
837 Fault: New insights into structural heterogeneity along a continental strike-slip fault, *Geophysi-
838 cal Research Letters*, **44**(5), 2186–2193.
- 839 Papaleo, E., Cornwell, D., & Rawlinson, N., 2018. Constraints on North Anatolian Fault Zone
840 Width in the Crust and Upper Mantle From S-Wave Teleseismic Tomography, *Journal of Geo-
841 physical Research: Solid Earth*, **123**(4), 2908–2922.
- 842 Paul, A., Karabulut, H., Mutlu, A. K., & Salaün, G., 2014. A comprehensive and densely sampled
843 map of shear-wave azimuthal anisotropy in the Aegean-Anatolia region, *Earth and Planetary*

- 844 *Science Letters*, **389**, 14–22.
- 845 Peng, Z. & Ben-Zion, Y., 2004. Systematic analysis of crustal anisotropy along the Karadere-
846 Düzce branch of the North Anatolian fault, *Geophysical Journal International*, **159**(1), 253–
847 274.
- 848 Polat, G., Özel, N. M., & Koulakov, I., 2016. Investigating P- and S-wave velocity structure be-
849 neath the Marmara region (Turkey) and the surrounding area from local earthquake tomography
850 the Next Marmara Earthquake: Disaster Mitigation, Recovery and Early Warning 4. *Seismology,*
851 *Earth, Planets and Space*, **68**(1), 132.
- 852 Reilinger, R., McClusky, S., Vernant, P., Lawrence, S., Ergintav, S., Cakmak, R., Ozener, H.,
853 Kadirov, F., Guliev, I., Stepanyan, R., Nadariya, M., Hahubia, G., Mahmoud, S., Sakr, K., Ar-
854 Rajehi, A., Paradissis, D., Al-Aydrus, A., Prilepin, M., Guseva, T., Evren, E., Dmitrotsa, A.,
855 Filikov, S., Gomez, F., Al-Ghazzi, R., & Karam, G., 2006. GPS constraints on continental
856 deformation in the Africa-Arabia-Eurasia continental collision zone and implications for the
857 dynamics of plate interactions, *Journal of Geophysical Research*, **111**(B05411).
- 858 Revenaugh, J., 1995. Relation of the 1992 Landers, California, earthquake sequence to seismic
859 scattering, *Science*, **270**(5240), 1344–1347.
- 860 Robertson, A. H. & Ustaömer, T., 2004. Tectonic evolution of the intra-pontide suture zone in
861 the Armutlu Peninsula, NW Turkey, *Tectonophysics*, **381**, 175 – 209.
- 862 Rondenay, S., 2009. Upper Mantle Imaging with Array Recordings of Converted and Scattered
863 Teleseismic Waves, *Surveys in Geophysics*, **30**(4-5), 377–405.
- 864 Ryberg, T. & Weber, M., 2000. Receiver function arrays: a reflection seismic approach, *Geo-*
865 *physical Journal International*, **141**(1), 1–11.
- 866 Salah, M. K., Sahin, S., & Kaplan, M., 2007. Seismic Velocity Structure along the Weestern
867 Segment of the North Anatolian Fault Zone Imaged by Seismic Tomography, *Bull. Earthqu.*
868 *Res. Inst.*, **82**(3), 209–223.
- 869 Salaün, G., Pedersen, H. A., Paul, A., Farra, V., Karabulut, H., Hatzfeld, D., Papazachos, C.,
870 Childs, D. M., & Pequegnat, C., 2012. High-resolution surface wave tomography beneath the
871 Aegean-Anatolia region: constraints on upper-mantle structure, *Geophysical Journal Interna-*

- 872 *tional*, **190**(1), 406–420.
- 873 Sato, H., Fehler, M. C., & Maeda, T., 2012. *Seismic wave propagation and scattering in the*
874 *heterogeneous earth: Second edition*, Springer-Verlag Berlin Heidelberg.
- 875 Şengör, A., Tüysüz, O., İmren, C., Sakiñç, M., Eyidoğan, H., Görür, N., LePichon, X., & Rangin,
876 C., 2005. The North Anatolian Fault: a New Look, *Annual Review of Earth and Planetary*
877 *Sciences*, **33**(1), 37–112.
- 878 Stein, R. S., Barka, A. A., & Dieterich, J. H., 1997. Progressive failure on the North Anatolian
879 fault since 1939 by earthquake stress triggering, *Geophysical Journal International*, **128**, 594–
880 604.
- 881 Stern, T. A. & McBride, J. H., 1998. Seismic exploration of continental strike-slip zones, *Tectono-*
882 *physics*, **286**(1-4), 63–78.
- 883 Tank, S. B., Honkura, Y., Ogawa, Y., Matsushima, M., Oshiman, N., Tunçer, M. K., Çelik, C.,
884 Tolak, E., & Işıkara, A. M., 2005. Magnetotelluric imaging of the fault rupture area of the 1999
885 İzmit (Turkey) earthquake, *Physics of the Earth and Planetary Interiors*, **150**(1-3), 213–225.
- 886 Taylor, G., Rost, S., & Houseman, G., 2016. Crustal imaging across the North Anatolian Fault
887 Zone from the autocorrelation of ambient seismic noise, *Geophysical Research Letters*, **43**,
888 2502–2509.
- 889 Taylor, G., Rost, S., Houseman, G., & Hillers, G., 2019a. Near-surface structure of the North
890 Anatolian Fault zone from Rayleigh and Love wave tomography using ambient seismic noise,
891 *Solid Earth*, **10**(2), 363–378.
- 892 Taylor, G., Thompson, D. A., Cornwell, D., & Rost, S., 2019b. Interaction of the Cyprus/Tethys
893 slab with the mantle transition zone beneath Anatolia, *Geophysical Journal International*,
894 **216**(3), 1665–1674.
- 895 Tibi, R., Bock, G., Xia, Y., Baumbach, M., Grosser, H., Milkereit, C., Karakisa, S., Zünbül, S.,
896 Kind, R., & Zschau, J., 2001. Rupture processes of the 1999 August 17 İzmit and November 12
897 Düzce (Turkey) earthquakes, *Geophysical Journal International*, **144**(2), F1–F7.
- 898 Van der Lee, S. & Nolet, G., 1997. Seismic image of the subducted trailing fragments of the
899 Farallon plate, *Nature*, **386**(6622), 266–269.

- 900 Vanacore, E. A., Taymaz, T., & Saygin, E., 2013. Moho structure of the Anatolian Plate from
901 receiver function analysis, *Geophysical Journal International*, **193**(1), 329–337.
- 902 Vauchez, A., Tommasi, A., & Mainprice, D., 2012. Faults (shear zones) in the Earth’s mantle,
903 *Tectonophysics*, **558-559**, 1–27.
- 904 Vinnik, L., 1977. Detection of waves converted from P to SV in the mantle, *Physics of the Earth
905 and Planetary interiors*, **15**, 39–45.
- 906 Weber, M., Abu-Ayyash, K., Abueladas, A., Agnon, A., Al-Amoush, H., Babeyko, A., Bartov, Y.,
907 Baumann, M., Ben-Avraham, Z., Bock, G., Bribach, J., El-Kelani, R., Förster, A., Förster, H.-J.,
908 Frieslander, U., Garfunkel, Z., Grunewald, S., Götze, H. J., Haak, V., Haberland, C., Hassouneh,
909 M., Helwig, S., Hofstetter, A., Jäckel, K.-H., Kesten, D., Kind, R., Maercklin, N., Mechie, J.,
910 Mohsen, A., Neubauer, F. M., Oberhänsli, R., Qabbani, I., Ritter, O., Rumpker, G., Rybakov, M.,
911 Ryberg, T., Scherbaum, F., Schmidt, J., Schulze, A., Sobolev, S., Stiller, M., Thoss, H., Weck-
912 mann, U., & Wylegalla, K., 2004. The crustal structure of the Dead Sea Transform, *Geophysical
913 Journal International*, **156**, 655–681.
- 914 Willis, K., Houseman, G. A., Evans, L., Wright, T., & Hooper, A., 2019. Strain localization by
915 shear heating and the development of lithospheric shear zones, *Tectonophysics*, **764**, 62–76.
- 916 Wu, R. & Aki, K., 1985. Scattering Characteristics of Elastic-Waves by an Elastic Heterogeneity,
917 *Geophysics*, **50**(4), 582–595.
- 918 Yan, Z. & Clayton, R. W., 2007. A notch structure on the Moho beneath the Eastern San Gabriel
919 Mountains, *Earth and Planetary Science Letters*, **260**(3-4), 570–581.
- 920 Yilmaz, Ö., 2001. *Seismic Data Analysis*, Society of Exploration Geophysicists.
- 921 Yolsal-Çevikbilen, S., Biryol, C. B., Beck, S., Zandt, G., Taymaz, T., Adıyaman, H. E., & Özacar,
922 A. A., 2012. 3-D crustal structure along the North Anatolian Fault Zone in north-central Anato-
923 lia revealed by local earthquake tomography, *Geophysical Journal International*, **188**(3), 819–
924 849.
- 925 Zhang, J. & Frederiksen, A. W., 2013. 3-D crust and mantle structure in southern Ontario, Canada
926 via receiver function imaging, *Tectonophysics*, **608**, 700–712.
- 927 Zor, E., Sandvol, E., Gürbüz, C., Türkelli, N., Seber, D., & Barazangi, M., 2003. The crustal

928 structure of the East Anatolian plateau (Turkey) from receiver functions, *Geophysical Research*
929 *Letters*, **30**(24).